JGR Solid Earth

RESEARCH ARTICLE
10.1029/2025JB031715

Linking the Spin Transition of Ferric Iron in δ-(Al,Fe)OOH to Water Storage in the Lower Mantle

Johannes Buchen[1,2,3], Olivia S. Pardo[2], Vasilije V. Dobrosavljevic[2,4], Wolfgang Sturhahn[2], Takayuki Ishii[1,5], Stella Chariton[6], Eran Greenberg[6,7], Thomas S. Toellner[8], and Jennifer M. Jackson[2]

[1]Bayerisches Geoinstitut, Universität Bayreuth, Bayreuth, Germany, [2]Seismological Laboratory, California Institute of Technology, Pasadena, CA, USA, [3]Department of Earth Sciences, University of Oxford, Oxford, UK, [4]Now at Earth and Planets Laboratory, Carnegie Institution for Science, Washington, DC, USA, [5]Now at Institute for Planetary Materials, Okayama University, Misasa, Japan, [6]GSECARS, The University of Chicago, Chicago, IL, USA, [7]Now at Applied Physics Division, Soreq NRC, Yavne, Israel, [8]Advanced Photon Source, Argonne National Laboratory, Argonne, IL, USA

Key Points:

- We derive the thermal equation of state and construct a thermodynamic model for the spin transition of ferric iron in delta-(Al,Fe)OOH
- The spin transition of ferric iron in the Fe-Al-component of phase H reduces the activity of water in a coexisting melt
- The spin transition of ferric iron may raise the thermal stability of phase H solid solutions in iron-rich regions of the lower mantle

Supporting Information:

Supporting Information may be found in the online version of this article.

Correspondence to:

J. Buchen,
johannes.buchen@uni-bayreuth.de

Citation:

Buchen, J., Pardo, O. S., Dobrosavljevic, V. V., Sturhahn, W., Ishii, T., Chariton, S., et al. (2025). Linking the spin transition of ferric iron in δ-(Al,Fe)OOH to water storage in the lower mantle. *Journal of Geophysical Research: Solid Earth*, *130*, e2025JB031715. https://doi.org/10.1029/2025JB031715

Received 3 APR 2025
Accepted 28 JUL 2025

Author Contributions:

Conceptualization: Johannes Buchen, Jennifer M. Jackson
Data curation: Johannes Buchen
Formal analysis: Johannes Buchen
Funding acquisition: Johannes Buchen, Jennifer M. Jackson
Investigation: Johannes Buchen, Olivia S. Pardo, Vasilije V. Dobrosavljevic, Wolfgang Sturhahn, Takayuki Ishii, Jennifer M. Jackson
Methodology: Johannes Buchen, Wolfgang Sturhahn, Jennifer M. Jackson
Project administration: Johannes Buchen, Jennifer M. Jackson

Abstract As the most massive geochemical reservoir, the lower mantle affects the Earth's budget of volatile elements, including hydrogen or H_2O. The properties of minerals in the lower mantle are further affected by changes in the electronic configurations of iron cations, that is, by spin transitions. The feedback between spin transitions and potential storage of H_2O in solid hydrous phases in the lower mantle, however, remains unexplored. By combining high-pressure nuclear resonant inelastic X-ray scattering and high-pressure high-temperature X-ray diffraction experiments, we constrained the thermal equation of state of δ-(Al,Fe)OOH, a member of the phase H solid solution. Based on the derived thermal equation of state of δ-(Al,Fe)OOH and the underlying thermodynamic model, we calculate the excess Gibbs free energy that arises from the spin transition of ferric iron in this compound and evaluate the effect on phase equilibria. The results of our analysis show that the spin transition of ferric iron in phase H may significantly reduce the thermodynamic activity and hence the concentration of H_2O in a coexisting hydrous melt. As a consequence, nominally anhydrous minerals of the lower mantle may become dehydrated in the presence of phase H. Our analysis further suggests that, under certain conditions, the spin transition may expand the thermal stability of Fe^{3+}-bearing phase H and create a geochemical link between the storage of H_2O in phase H and ferric iron in the lower mantle.

Plain Language Summary The lower mantle forms the Earth's most massive subunit and may store H_2O in the minerals that form the rocks of the lower mantle. At the pressures of the lower mantle, the valence electrons of iron cations in minerals may change their arrangement, which has consequences for the energy of the affected minerals. Our study explores whether these electronic changes may affect the storage of H_2O in δ-(Al,Fe)OOH, which is a hydrous compound that may form in rocks of the lower mantle. We used high-pressure experiments to determine the changes in energy that arise from electronic rearrangements in trivalent iron cations in δ-(Al,Fe)OOH and derived a thermodynamic model to describe these changes. We found that the electronic rearrangement reduces the energy of the compound δ-(Al,Fe)OOH and therefore promotes storage of H_2O in this compound at pressures and temperatures of the lower mantle. Furthermore, the electronic rearrangement may raise the temperature at which the compound δ-(Al,Fe)OOH releases the stored H_2O. Our findings have implications for the storage of H_2O in the lower mantle as they suggest a connection between the trivalent iron cations in δ-(Al,Fe)OOH and the capability to store H_2O in this compound.

1. Introduction

Basaltic magmas generated at deep-rooted volcanic hotspots contain more H_2O than magmas produced along mid-ocean ridges (Bolfan-Casanova, 2005; Dixon et al., 2002; Hirschmann, 2006). In some locations, elevated magmatic H_2O concentrations are associated with high $Fe^{3+}/\Sigma Fe$ ratios (Brounce et al., 2017; Moussallam et al., 2019). These and other geochemical observations of plume-related magmatic activity are commonly attributed to geochemical reservoirs that reside in the Earth's lower mantle and are being sampled by rising plumes (Brounce et al., 2017; Moussallam et al., 2019; Weis et al., 2023). The Earth's lower mantle and the source regions of plumes in particular might therefore be a geochemical reservoir for H_2O. The important role of the lower mantle for the Earth's global H_2O budget has been pointed out in recent review articles together with considerable

Resources: Takayuki Ishii, Stella Chariton, Eran Greenberg, Thomas S. Toellner
Software: Wolfgang Sturhahn
Supervision: Jennifer M. Jackson
Validation: Wolfgang Sturhahn, Jennifer M. Jackson
Visualization: Johannes Buchen
Writing – original draft: Johannes Buchen
Writing – review & editing: Johannes Buchen, Olivia S. Pardo, Vasilije V. Dobrosavljevic, Wolfgang Sturhahn, Takayuki Ishii, Stella Chariton, Eran Greenberg, Thomas S. Toellner, Jennifer M. Jackson

uncertainties on the estimated amounts of H_2O stored in the lower mantle (Andrault & Bolfan-Casanova, 2022; Karato et al., 2020; Ohtani, 2021; Ohtani & Ishii, 2024; Peslier et al., 2017).

In contrast to the exceptionally high H_2O storage capacity (~1 wt-% H_2O) of nominally anhydrous minerals (NAMs) in ultramafic rocks of the mantle transition zone (Bolfan-Casanova, 2005; H. Fei & Katsura, 2020; Kohlstedt et al., 1996, 2021), the most abundant NAMs in ultramafic rocks of the lower mantle, bridgmanite and ferropericlase, incorporate much less H_2O (Bolfan-Casanova et al., 2000, 2002, 2003; Z. Liu et al., 2021; Panero et al., 2015). The highest reported H_2O contents in bridgmanite of about 0.1 wt-% H_2O (Fu et al., 2019; Litasov et al., 2003) are, however, highly controversial. While the most abundant NAMs of the lower mantle may store a rather limited amount of H_2O, the stability fields of hydrous high-pressure phases extend to pressures and temperatures that may be compatible with colder parts of the lower mantle (Komabayashi & Omori, 2006; Nishi et al., 2014; Ohtani, 2015, 2021; Ohtani et al., 2004).

The results of high-pressure experiments indicate that at pressures above 30 GPa H_2O might be retained in high-pressure oxyhydroxide phases such as $MgSiO_2(OH)_2$ (phase H) (Nishi et al., 2014; Ohtani et al., 2014) and δ-AlOOH (δ-phase) (Duan et al., 2018; Piet et al., 2020; Sano et al., 2008). Solid solutions of these two endmembers coexisted with Al-bearing bridgmanite or post-perovskite in experiments at pressures and temperatures of the lower mantle (Ishii, Ohtani, & Shatskiy, 2022; Ohira et al., 2014; Walter et al., 2015). In the following, we will refer to the high-pressure oxyhydroxide solid solution as phase H solid solution or briefly as phase H. Similar to the system $MgSi_2O_4(OH)_2$–$Al_2SiO_4(OH)_2$ (phase D) (Ghosh & Schmidt, 2014; Pamato et al., 2014), the coupled substitution of Mg^{2+} and Si^{4+} by two Al^{3+} extends the stability of phase H to higher pressures and temperatures, approaching the temperatures of the ambient mantle with increasing pressure (Ishii, Ohtani, & Shatskiy, 2022; Ohira et al., 2014; Walter et al., 2015). The effect of iron on the stability limit of the phase H solid solution, however, remains largely unconstrained.

Iron is incorporated into phase H mostly as the component FeOOH, that is, as ferric iron (Fe^{3+}) (Nishi et al., 2015, 2017; Xu et al., 2019; Yuan et al., 2019). The crystal structures of $MgSiO_2(OH)_2$ (phase H), δ-AlOOH, and the high-pressure polymorph ε-FeOOH are very similar to each other and are all based on the $CaCl_2$ crystal structure type (Bindi et al., 2014; Chenavas et al., 1973; Komatsu et al., 2006; Nishi et al., 2014; Pernet et al., 1975; Suzuki, 2010; Suzuki et al., 2000), which is a distorted variant of the rutile structure. Despite small structural differences at low pressures, the endmembers $MgSiO_2(OH)_2$, δ-AlOOH, and ε-FeOOH as well as intermediate compositions of the phase H solid solution adopt a crystal structure with space group symmetry *Pnnm* at pressures of the lower mantle (Gleason et al., 2013; Nishi et al., 2018; Ohira et al., 2019; Sano-Furukawa et al., 2009, 2018; Strozewski et al., 2023; Thompson et al., 2020). In this structure, the metal cations including Fe^{3+} are octahedrally coordinated by oxygen anions. As a result of the octahedral coordination, ferric iron in phase H solid solution goes through a spin transition upon compression to pressures of 30–60 GPa, with the exact transition pressure depending on composition (Gleason et al., 2013; Nishi et al., 2019; Ohira et al., 2019; Strozewski et al., 2023; Su, Zhao, Xu, et al., 2021). Whether and how the spin transition of ferric iron in phase H affects its stability and hence capacity to store H_2O in the lower mantle remains unexplored.

The main driving force for spin transitions of Fe^{3+} cations in octahedral coordination is the volume reduction that is associated with the change in the electronic configuration of the *d* electrons of the Fe^{3+} cations from a high-spin to a low-spin configuration. As a result, the pressure of the spin transition depends on the volume of the coordination environment of Fe^{3+} cations which, in turn, changes with the composition of a solid solution. For the endmember ε-FeOOH, the pressure of the spin transition was determined to be about 65 GPa by first-principles calculations based on density functional theory (DFT) (Gleason et al., 2013). High-pressure experiments on the same composition indicate a pressure interval of the spin transition between 40 and 60 GPa (Gleason et al., 2013; Nishi et al., 2019; Thompson et al., 2020). In solid solutions of δ-AlOOH and ε-FeOOH with ratios of Fe/(Al+Fe) < 0.5, which are more relevant for typical rock compositions of the lower mantle, the pressure interval of the spin transition shifts to lower pressures of 30–50 GPa (Ohira et al., 2019; Strozewski et al., 2023; Su, Zhao, Xu, et al., 2021).

In contrast to the octahedral coordination of Fe^{3+} in phase H, ferric iron in bridgmanite prefers the larger A site over the octahedral B site when incorporated together with aluminum as the component $FeAlO_3$ and remains in the high-spin state up to the highest pressures of the lower mantle (Glazyrin et al., 2014; Hsu et al., 2012; Lin et al., 2016). The very limited information on the partitioning of Fe^{3+} between bridgmanite and the phase H solid

solution indicates a preference of Fe^{3+} to enter phase H (Nishi et al., 2015; Yuan et al., 2019). While iron appears to have a small effect on the dehydration temperatures of phase H at pressures between 30 and 50 GPa (Nishi et al., 2015), Fe-Al-bearing phase H was found together with Fe-Al-bearing bridgmanite and/or post-perovskite in experiments at pressures above 100 GPa and at temperatures up to 2400 K (Yuan et al., 2019). At pressures above 110 GPa, however, the FeOOH component appears to exsolve from phase H and to form a pyrite-structured phase (Nishi et al., 2017; Yuan et al., 2019).

Previous experimental studies have investigated the stability limits of phase H, δ-AlOOH, or intermediate members of the phase H solid solution at pressures above 50 GPa by constraining the dehydration temperatures of samples embedded in alkaline salts (NaCl, KCl) or noble gases as pressure-transmitting media (Duan et al., 2018; Ohira et al., 2014; Ohtani et al., 2014; Piet et al., 2020; Yuan et al., 2019). Phase equilibria and especially dehydration temperatures determined on phase H samples embedded in salts or noble gases, however, may not be directly transferable to the stability of the phase H solid solution in lower-mantle rocks, for instance, because the thermodynamic activity of H_2O and other chemical components was not buffered or known. As an alternative to dehydration experiments, the thermodynamic properties of phase H solid solutions may be determined and integrated into thermodynamic models to evaluate the stability of the phase H solid solution at pressures and temperatures of the lower mantle.

In this study, we determined the thermal equation of state (EOS) of δ-(Al,Fe)OOH by combining the results of high-pressure nuclear resonant inelastic X-ray scattering (NRIXS) experiments with those of high-pressure high-temperature X-ray diffraction (XRD) experiments. The composition of our δ-(Al,Fe)OOH sample falls along the binary branch AlOOH–FeOOH of the ternary phase H solid solution with the additional endmember $MgSiO_2(OH)_2$. Our description of the thermal EOS allows for a quantitative assessment of changes in free energy that arise from the spin transition of ferric iron in the phase H solid solution. Based on this assessment, we show that the spin transition has a significant effect on the thermal stability of Fe^{3+}-bearing phase H and reduces the activity of H_2O that is needed to form phase H in a hydrous rock of the lower mantle.

2. Experimental Methods

2.1. Sample Synthesis and Composition

Crystals of δ-(Al,Fe)OOH were synthesized by annealing a mixture of $Al(OH)_3$ and $^{57}Fe_2O_3$ powders in a multi-anvil press at 27 GPa and 1500 K. Details of the synthesis procedure and sample characterization have been published elsewhere (Buchen et al., 2021; Kawazoe et al., 2017). To enhance the signal-to-noise ratio and to reduce collection times of high-pressure NRIXS spectra (see below), we used Fe_2O_3 powder enriched with the Mössbauer-active isotope ^{57}Fe to a concentration of $^{57}Fe/\Sigma Fe = 96\%$. The composition of eight δ-(Al,Fe)OOH grains was determined by electron microprobe analysis and can be described by the ratio $Fe/(Al+Fe) = 0.13(2)$ or the formula $Al_{0.87}Fe_{0.13}OOH$. All samples used in this study were produced by the same synthesis experiment.

2.2. High-Pressure X-Ray Diffraction Experiments

Symmetric diamond anvil cells (DAC) were prepared using diamond anvils with 250-μm culets beveled to 300 μm. The pressure chambers of the DACs were sealed with rhenium gaskets that were pre-indented to a thickness of 45–55 μm and drilled with an electric discharge machine. Grains of δ-(Al,Fe)OOH were repeatedly crushed between the tips of two diamond anvils to obtain a fine-grained powder. Flakes of this powder were loaded into the pressure chambers of the DACs along with other materials as described below. Photomicrographs of the pressure chambers of all three DACs loaded for high-pressure X-ray diffraction (XRD) experiments are shown in Figure S1 in Supporting Information S1.

For high-pressure XRD experiments at room temperature, a flake of the δ-(Al,Fe)OOH powder was placed inside the pressure chamber of a DAC together with a ruby sphere and gold (Au) powder for pressure determination (Dewaele et al., 2008; Y. Fei et al., 2007). Pre-compressed helium was loaded as a pressure-transmitting medium. For XRD experiments at combined high pressures and high temperatures, powder of δ-(Al,Fe)OOH, a ruby sphere, and gold powder were embedded in powder of $Al(OH)_3$ inside the pressure chambers of two symmetric DACs.

We used $Al(OH)_3$ as pressure-transmitting medium and thermal insulation for experiments at simultaneously high pressures and high temperatures with the intention of buffering the activity of H_2O inside the pressure chamber of the DAC. If heated beyond its thermal stability, $Al(OH)_3$ releases H_2O and buffers the activity of H_2O in the pressure chamber at a high value which, in turn, prevents the δ-(Al,Fe)OOH sample from dehydrating. $Al(OH)_3$ becomes progressively amorphous upon compression (H. Liu et al., 2004) and is not expected to absorb the radiation of the near-infrared laser used to heat the sample and gold powder. As a result, $Al(OH)_3$ did not contribute significantly to the recorded XRD patterns and effectively insulated the sample and gold powder from the diamond anvils during laser heating.

All high-pressure XRD patterns were collected at beamline 13-ID-D operated by GeoSoilEnviroCARS (GSE-CARS) at the Advanced Photon Source at Argonne National Laboratory. The X-ray beam with a photon energy of 37.078 keV (0.33438 Å) was focused to an area of 2.5 μm × 3.5 μm at the sample position. Diffracted X-rays were recorded on a Dectris Pilatus 1M CdTe area detector. The detector distance and diffraction geometry were calibrated using a LaB_6 reference material. For high-pressure XRD experiments at room temperature, the DAC was connected to an inflatable metallic membrane for remote pressure control. XRD patterns were collected with exposure times of 4 or 5 s. To increase the number of grains contributing to XRD patterns, the DAC was rotated about the vertical axis from $-3°$ to $+3°$ during the acquisition of XRD patterns.

For XRD experiments at simultaneously high pressures and high temperatures, the sample and gold powders were heated inside the pressure chambers of DACs using the double-sided laser-heating setup installed at beamline 13-ID-D. During laser heating, thermal emission spectra of the heated area were recorded through both diamond anvils and fit to gray-body emission curves using the software T-Rax (Holtgrewe et al., 2019; Prescher, 2016) to determine the temperature of the heated area. For a typical heating cycle, we first recorded an XRD pattern at room temperature with an exposure time of 5 s. We then irradiated the same area within the pressure chamber with the infrared lasers from both sides while recording another XRD pattern for 5 s. During the X-ray exposure, we collected a series of thermal emission spectra. After switching off the laser, we collected another XRD pattern at room temperature. The temperatures of subsequent heating cycles were adjusted by changing the laser output power. The temperature assigned to each high-pressure high-temperature XRD pattern corresponds to the average temperature from all emission spectra collected during the acquisition of the XRD pattern at high temperature. The associated uncertainty was estimated by the standard deviation of the same set of temperatures.

2.3. Analysis of X-Ray Diffraction Patterns

The images of XRD patterns as recorded by the area detector were read into the software DIOPTAS (Prescher, 2019–2020; Prescher & Prakapenka, 2015) and integrated to profiles of intensity as a function of the diffraction angle 2θ (Buchen, Pardo, Dobrosavljevic, Chariton, et al., 2025). Coherent stacks of diffraction profiles were then analyzed and corrected for common background intensities using the software MINUTI (Sturhahn, 2021a). Lattice parameters and unit cell volumes of δ-(Al,Fe)OOH and gold were extracted from the diffraction profiles by matching calculated profiles to the observed profiles using the software FullProf (Rodríguez-Carvajal, 1993, 2020). Examples of profile-matching results are shown in Figure 1.

X-ray reflections of δ-(Al,Fe)OOH were indexed according to the space group symmetry *Pnnm* (Ohira et al., 2019; Sano-Furukawa et al., 2009). The number of reflections that were included in the profile-matching refinements ranged from 52 at low pressures to 38 at the highest pressure for XRD patterns of δ-(Al,Fe)OOH compressed in helium and at room temperature (Figure 1a). Additional reflections in these XRD patterns were assigned to gold, rhenium, and helium and included in the profile-matching procedure as well. In addition to reflections of gold, between 41 and 45 reflections of δ-(Al,Fe)OOH were included in the analysis of XRD patterns that were recorded in combination with laser heating (Figure 1b). Note that the accessible range of diffraction angles begins at $2\theta = 8°$ for laser-heating experiments.

The unit cell volumes of gold, combined with temperatures for XRD experiments at simultaneously high pressures and high temperatures, were used to calculate pressures from the equation of state (EOS) of gold (Y. Fei et al., 2007). Uncertainties in unit cell volumes and temperatures were propagated into uncertainties on pressures. Unit cell volumes of δ-(Al,Fe)OOH and gold are compiled together with the respective (thermal) pressures and temperatures in Tables S1 and S2.

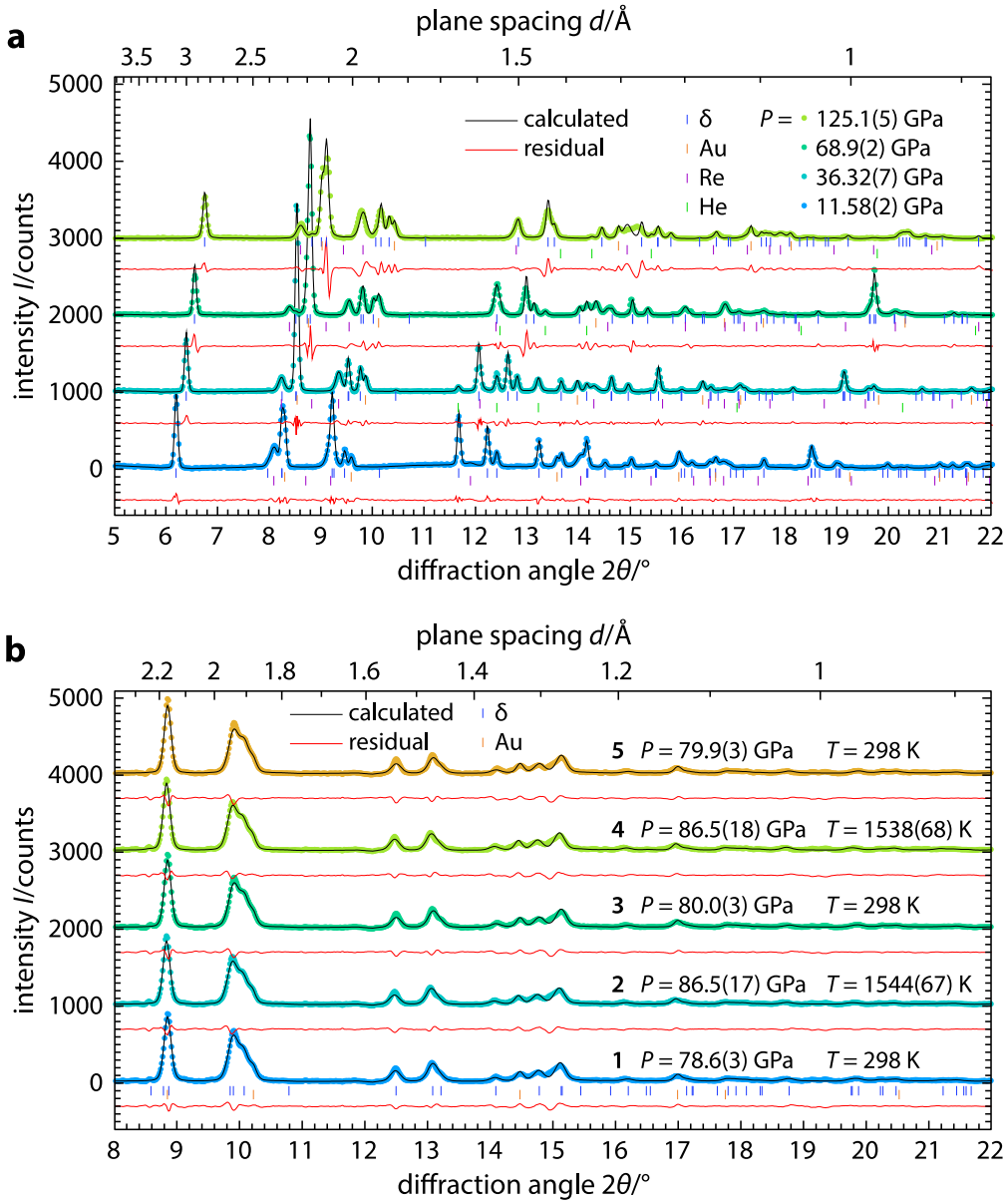

Figure 1. Analysis of high-pressure X-ray diffraction patterns. (a) Examples of X-ray diffraction patterns recorded at different pressures and room temperature. (b) Example of a series of X-ray diffraction patterns recorded at simultaneously high pressures and high temperatures during a typical cycle of laser heating. The sequence of the patterns is indicated by the numbers 1–5. X-ray diffraction patterns were corrected for background intensities and fit to calculated diffraction profiles by refining the lattice and peak shape parameters of δ-$Al_{0.87}$ $Fe_{0.13}$OOH (δ), gold (Au, pressure calibrant), rhenium (Re, gasket material, only in (a)), and helium (He, pressure-transmitting medium, only in (a)).

To calculate the thermal pressures P_{TH} acting on δ-(Al,Fe)OOH during laser heating, we paired each high-temperature (hot, H) combination P_H–V_H–T_H of pressure P, unit cell volume V, and temperature T with the room-temperature (cold, C) combination P_C–V_C–T_C recorded immediately before or after the hot combination. The resulting pairs of pressures P_H and P_C were shifted to make the cold pressure P_C fall onto the room-temperature compression curve of δ-(Al,Fe)OOH determined in helium while leaving the difference $(P_H - P_C)$ unchanged. This procedure corrects for systematic offsets in pressure caused by deviatoric stresses in the $Al(OH)_3$ pressure-transmitting medium but retains any changes in pressure and volume that arise from heating. The thermal pressure P_{TH} was then calculated by subtracting the cold pressure at the hot volume

$P(V_H, T_C)$ as calculated from our room-temperature EOS of δ-(Al,Fe)OOH from the corrected hot pressure P^*_H, that is, $P_{TH} = P^*_H(V_H, T_H) - P(V_H, T_C)$ with $T_C = 298$ K.

2.4. High-Pressure Nuclear Resonant Inelastic X-Ray Scattering Experiments

Grains of δ-(Al,Fe)OOH were cleaved into smaller pieces with a razor blade and rinsed in acetone. A crystal fragment was placed inside the pressure chamber of a panoramic diamond anvil cell (panDAC) together with a ruby sphere for pressure determination. To keep the number density of ^{57}Fe atoms in the sample as high as possible so as to maximize the photon yield of NRIXS experiments, we used a crystal fragment of δ-(Al,Fe)OOH instead of a powder. Pre-compressed helium was loaded as a pressure-transmitting medium. For the panDAC, we used diamond anvils with culet diameters of 250 μm beveled to 300 μm. The pressure chamber was prepared from a beryllium disk pre-indented to a thickness of about 50 μm and drilled with an electric discharge machine. To further stabilize the beryllium gasket, we lined the pressure chamber with a mixture of boron powder and epoxy resin. Photomicrographs of the pressure chamber taken at different compression steps are shown in Figure S2 in Supporting Information S1.

After compression to about 20 GPa, we noted a contraction of the pressure chamber caused by lateral spreading of the boron–epoxy lining, which may have resulted in (partial) loss of helium from the pressure chamber. As a result, the ruby sphere was enclosed between the sample and the boron–epoxy lining, which in turn led to a deterioration of ruby spectra with increasing pressure. We therefore decided to determine pressures from Raman spectra of the diamond anvils (Akahama & Kawamura, 2006). For consistency, we corrected pressures derived from ruby spectra (Dewaele et al., 2008) based on a cross-calibration between both pressure scales that we established by measuring pressures on several other DACs, including another panDAC, with the same optical setup and using calibrations for both the ruby R_1 fluorescence line (Dewaele et al., 2008) and the Raman spectra of diamond anvils (Akahama & Kawamura, 2006).

Nuclear resonant inelastic X-ray scattering (NRIXS) spectra were collected at beamline 3-ID-B of the Advanced Photon Source at Argonne National Laboratory. The X-ray beam was focused to about 15 μm × 15 μm at the sample position and irradiated the sample through one of the diamond anvils. The energy of incident X-ray photons was tuned around the resonance energy of ^{57}Fe (14.4 keV) using a high-resolution monochromator and had a bandwidth of about 1 meV (Toellner, 2000). To record NRIXS spectra, the X-ray energy was scanned across the resonance energy of ^{57}Fe in steps of 0.25 meV while recording time-delayed fluorescence photons for 2–5 s at each step using three avalanche photodiodes (APD). The APDs were inserted into the radial apertures of the panDAC to detect fluorescence photons emitted by the sample after absorption events by ^{57}Fe atoms and transmitted through the beryllium gasket. The collection of a single NRIXS spectrum of adequate quality required scanning the relevant energy range 12–31 times with each scan taking about 1 hr. The recorded NRIXS spectra are shown in Figure 2.

2.5. Analysis of Nuclear Resonant Inelastic X-Ray Scattering Spectra

NRIXS spectra were compiled from sets of individual scans and processed using the software PHOENIX (Buchen, Pardo, Dobrosavljevic, Sturhahn, et al., 2025; Sturhahn, 2000, 2021b). After normalization, the projected partial phonon densities of states (p^3DOS) of ^{57}Fe atoms in δ-(Al,Fe)OOH was extracted from each spectrum (Sturhahn, 2004; Sturhahn & Kohn, 1999). The p^3DOS describes the energy distribution of those lattice vibrations (phonons) that displace ^{57}Fe atoms from their equilibrium positions in the crystal structure of δ-(Al,Fe)OOH. In addition, only displacements of ^{57}Fe atoms with a component along the X-ray wave vector contribute to the NRIXS spectrum. Since we used a crystal fragment in our high-pressure NRIXS experiments, our NRIXS spectra might be affected by the anisotropic displacement of ^{57}Fe atoms in δ-(Al,Fe)OOH (Buchen et al., 2021). Given the consistency with an existing set of p^3DOS on a similar composition of δ-(Al,Fe)OOH (Ohira et al., 2021) (Figure 4) and the unknown degree of anisotropy at high pressures, however, we assume that the p^3DOS extracted from our NRIXS spectra approximate the isotropic partial phonon densities of states reasonably well.

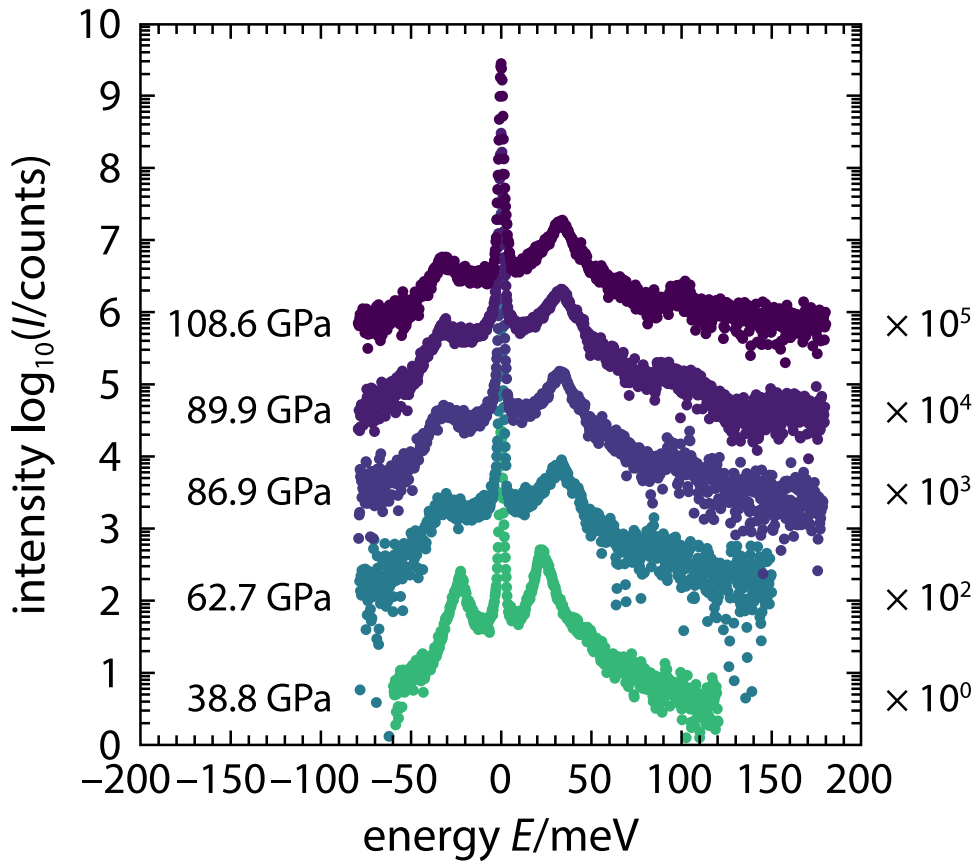

Figure 2. High-pressure nuclear resonant inelastic X-ray scattering (NRIXS) spectra of δ-$Al_{0.87}$ $Fe_{0.13}$OOH. NRIXS spectra of δ-$Al_{0.87}$ $Fe_{0.13}$OOH with $^{57}Fe/\Sigma Fe = 96\%$ were recorded at different pressures and room temperature. Spectra are vertically offset for clarity as indicated on the right.

3. Compression Behavior and Equation of State of δ-(Al,Fe)OOH

The unit cell volumes of δ-(Al,Fe)OOH solid solutions with different compositions are plotted as a function of pressure in Figure 3. We focus on compositions of δ-(Al,Fe)OOH with Fe/(Al+Fe) < 0.5 as these appear most relevant for typical rock compositions of the lower mantle. For consistency, Figure 3 shows compression data from experiments that used helium as pressure-transmitting medium. We note, however, that additional compression experiments on various δ-(Al,Fe)OOH compositions including the endmembers δ-AlOOH and ε-FeOOH have been performed using other pressure-transmitting media (Duan et al., 2018; Gleason et al., 2013; Nishi et al., 2019; Sano-Furukawa et al., 2009; Su, Zhao, Lv, et al., 2021; Thompson et al., 2020).

The comparison of our room-temperature compression data of δ-(Al,Fe)OOH with Fe/(Al+Fe) = 0.13 with data of δ-(Al,Fe)OOH with less (Ohira et al., 2019) or no ferric iron (Sano-Furukawa et al., 2009) clearly reveals a segment of enhanced volume reduction between 30 and 40 GPa that has previously been identified and attributed to the spin transition of ferric iron in δ-(Al,Fe)OOH with Fe/(Al+Fe) < 0.5 (Ohira et al., 2019; Strozewski et al., 2023; Su, Zhao, Lv, et al., 2021). The transition of Fe^{3+} cations from the high-spin to the low-spin state leads to a reduction of the effective ionic radius of Fe^{3+}. As a result, the unit cell volumes of δ-(Al,Fe)OOH with low-spin Fe^{3+} become similar to those of δ-AlOOH at pressures above 40 GPa.

3.1. Crystal-Field Model for the Spin Transition

To evaluate how the spin transition of Fe^{3+} affects the stability and phase equilibria of phase H solid solutions, we need an equation of state (EOS) for Fe^{3+}-bearing compositions that links the effect of the spin transition on the compression behavior to the changes in free energy that arise from the spin transition. Fitting separate EOS to the high-spin and low-spin segments of the compression curve does not capture the compression behavior across the

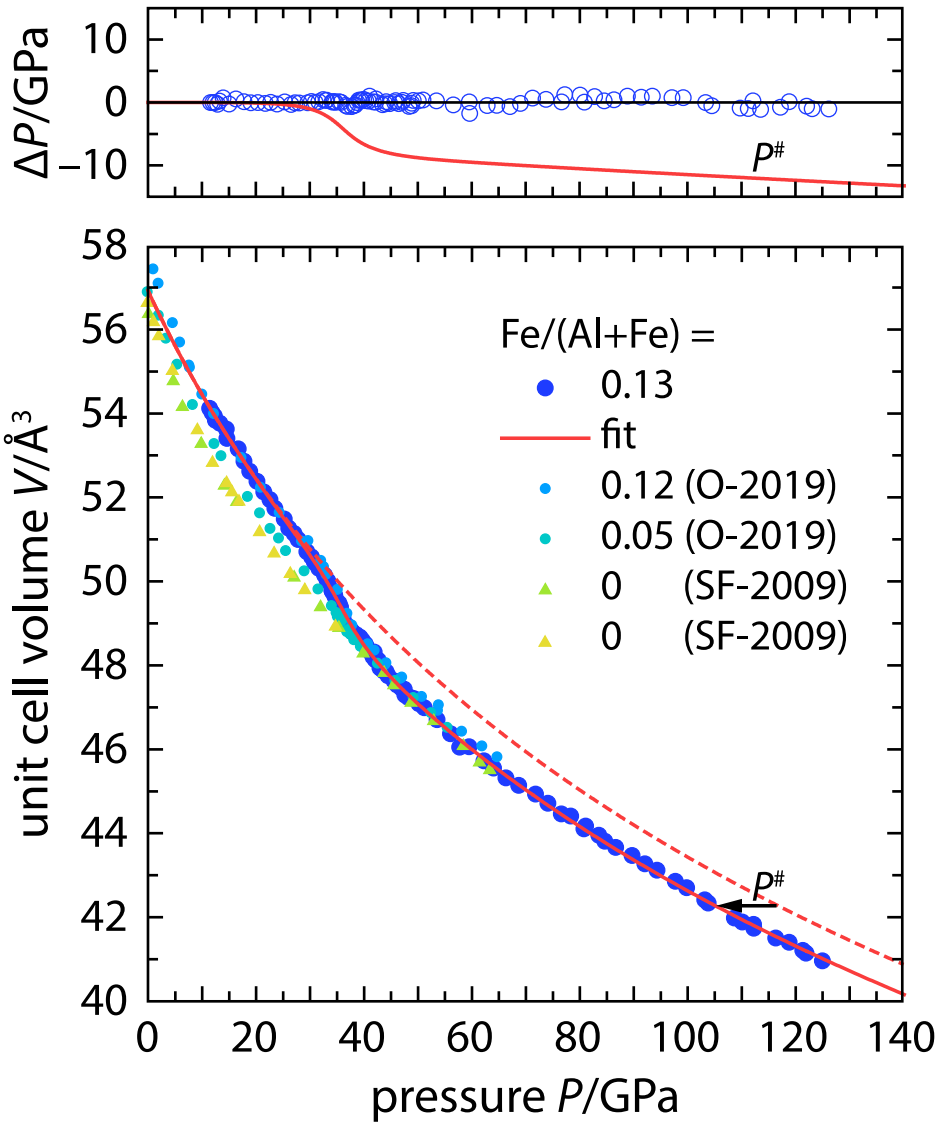

Figure 3. Room-temperature compression data of δ-(Al,Fe)OOH in helium with different iron contents as expressed by the ratio Fe/(Al+Fe). The *P*–*V* data for Fe/(Al+Fe) = 0.13 were fit to an equation of state that accounts for excess contributions to pressure due to the spin transition of ferric iron. The effect of the excess pressure $P^{\#}$ on the compression curve is indicated by the black arrow. The top panel shows the excess pressure $P^{\#}$ along with fitting residuals. Experimental uncertainties are within the sizes of the symbols. SF-2009: Sano-Furukawa et al. (2009), O-2019: Ohira et al. (2019).

pressure interval of the spin transition and may not combine the compression behavior along different segments into a single model for the free energy. As a consequence, this approach may not be used to evaluate the changes in free energy and other properties that arise from the spin transition.

In a recently proposed model, the changes in free energy and derived thermodynamic properties that arise from a spin transition are defined in terms of excess contributions (Buchen, 2021). These excess contributions capture the changes in thermodynamic properties that are exclusively attributable to the spin transition. Therefore, the model is ideally suited to evaluate the effect of the spin transition on phase equilibria and to differentiate the effect of the spin transition from the effects of other parameters or processes. The thermodynamic model for spin transitions proposed by Buchen (2021) is based on crystal-field theory and in many aspects similar to the model proposed by Sturhahn et al. (2005). The versatility of the model has been demonstrated by an analysis of spin transitions of iron cations in different minerals of the lower mantle (Buchen, 2021; Criniti et al., 2025).

The crystal-field model for the excess contributions is based on crystal-field theory and describes the Helmholtz free energy F_i of the d electron shell of an iron cation in a specific electronic state i and in the limit of a strong octahedral crystal field as:

$$F_i = z_{i1}\Delta + z_{i2}B + z_{i3}C - kT \ln m_i M_i. \tag{1}$$

The energy of a multi-electron state depends on the crystal-field splitting Δ and the Racah parameters B and C while the entropic term includes the spin multiplicity M_i and the orbital degeneracy m_i of the multi-electron state. The coefficients z_{i1}, z_{i2}, and z_{i3} have been tabulated for each d electron configuration and multi-electron state (Tanabe & Sugano, 1954). The crystal-field splitting Δ and the Racah parameters B and C are assumed to vary with volume V as:

$$\Delta = \Delta_0 \left(\frac{V_0}{V}\right)^{\delta/3} \tag{2}$$

$$B = B_0 \left(\frac{V_0}{V}\right)^{b/3} \tag{3}$$

$$C = C_0 \left(\frac{V_0}{V}\right)^{c/3} \tag{4}$$

with Δ_0, B_0, C_0, and V_0 being their respective values at ambient conditions.

At a given volume and temperature, the excess Helmholtz free energy $F^{\#}(V,T)$ per iron cation that arises from redistributing electrons over different electronic states with respect to their distribution at ambient conditions can then be expressed as:

$$F^{\#}(V,T) = \sum_i \Delta\phi_i F_i + dkT \sum_i \left(\phi_i \ln\phi_i - \phi_{i0} \ln \phi_{i0}\right). \tag{5}$$

where $\Delta\phi_i = \phi_i(V,T) - \phi_{i0}(V_0,T_0)$ is the change in the fraction $\phi_i(V,T)$ of Fe^{3+} cations with the electronic configuration i at the given volume and temperature with respect to the fraction $\phi_{i0}(V_0,T_0)$ at ambient conditions, and d is the number of d electrons per iron cation. The fractions ϕ_i at thermal equilibrium can be found from the conditions $(\partial F/\partial n_i)_{V,T,N} = 0$ for a micro-canonical ensemble with a total number of cations (or d electrons) N where $n_i = \phi_i N$ and $\sum_i \phi_i = 1$ (Buchen, 2021; Sturhahn et al., 2005). The excess contribution to pressure that arises from the spin transition then follows as:

$$P^{\#} = -(\partial F^{\#}/\partial V)_T. \tag{6}$$

For spin transitions at room temperature, the most relevant multi-electron states are the high-spin state and low-spin state. The high-spin and low-spin states of Fe^{3+} $\left(d^5\right)$ correspond to the states $^6A_1$ and $^2T_2$, respectively. The crystal-field model predicts, however, that a third state with intermediate spin $\left(^4T_1\right)$ may become populated by a significant fraction of Fe^{3+} cations at high temperatures (Buchen, 2021). Consequently, we therefore include all three states $^6A_1$, $^2T_2$, and $^4T_1$ in our analysis of excess contributions to thermodynamic properties.

The EOS $P(V,T)$ may now be split into different contributions:

$$P(V,T) = P_C(V,T_0) + P^{\#}(V,T) + P_{VIB}(V,T) \tag{7}$$

with the isothermal (cold) contribution $P_C(V,T_0)$, the excess contribution $P^{\#}(V,T)$ due to the redistribution of d electrons (spin transition), and the vibrational contribution $P_{VIB}(V,T)$ due to lattice vibrations. Both the excess contribution and the vibrational contribution contribute to thermal pressure P_{TH} at temperatures $T > T_0$. All parameters of the excess contribution, however, are temperature-independent and may be derived from room-temperature compression data. Since the spin transition broadens with increasing temperature, the impact on

Table 1
Isothermal Equation of State (EOS) Parameters of δ-(Al,Fe)OOH in Helium

		EOS parameters			Spin transition	
Fe/(Al+Fe)	EOS[a]	V_0 (Å^3)	K_0 (GPa)	K_0'	pressure[b] (GPa)	Reference
0	BM2	55.47(8)	219(3)	4	—	Sano-Furukawa et al. (2009)
0.05	BM3 (HS)	56.9(4)	149(25)	8(2)	35(1)	Ohira et al. (2019)
	BM2 (LS)	55.4(3)	223(11)	4		
0.12	BM3 (HS)	57.5(3)	155(22)	8(2)	36.1(7)	Ohira et al. (2019)
	BM2 (LS)	55.2(4)	241(14)	4		
0.13	BM3-CF	56.93(4)	205(3)	4.34(8)	36(1)	This study

Note. Values without uncertainties in parentheses were fixed. [a]BM2/BM3 = 2nd/3rd order Birch–Murnaghan EOS; HS = high spin; LS = low spin; BM3-CF = 3rd order Birch–Murnaghan EOS with crystal-field model. [b]The pressure at which the fractions of iron cations in the high-spin and low-spin states are equal.

the compression curve is more prominent at room temperature than at high temperatures. The parameters of the excess contribution, that is, of the crystal-field model, are therefore best derived from room-temperature P–V data.

3.2. Isothermal Equation of State of δ-(Al,Fe)OOH

We describe the room-temperature compression behavior of δ-(Al,Fe)OOH with Fe/(Al+Fe) = 0.13 by a third-order Birch–Murnaghan EOS, to which we add the room-temperature excess pressure $P^{\#}(V,T_0)$ that arises from the spin transition:

$$P(V,T_0)=\frac{1}{3}(1+2f)^{2/3}\left(9K_0f+\frac{27}{2}K_0\left(K_0'-4\right)f^2\right)+P^{\#}(V,T_0). \quad (8)$$

The finite strain f is calculated from the unit cell volume V as

$$f=\frac{1}{2}\left(\left(\frac{V_0}{V}\right)^{2/3}-1\right). \quad (9)$$

The unit cell volume V_0 at ambient conditions as well as the isothermal bulk modulus K_0 at ambient conditions and its pressure derivative K_0' are adjustable parameters.

By fitting Equation 8 to the experimental pressure–volume data of δ-(Al,Fe)OOH with Fe/(Al+Fe) = 0.13, we constrained the parameters of the isothermal EOS together with some of the crystal-field parameters that are needed to evaluate the excess pressure. While the crystal-field splitting Δ_0 at ambient conditions was derived from our fit, we fixed the Racah parameters B_0 and C_0 at ambient conditions as well their ratio C/B to values for Fe^{3+} derived from spectroscopic measurements, that is, B_0 = 655 cm^{-1} and C/B = 4.73 (Burns, 1993). We further found the exponent δ, which describes the volume scaling of the crystal-field splitting Δ, to be highly correlated with the corresponding exponent b (=c) for the Racah parameters. As a consequence, we fixed δ to 5, the value for approximating the coordinating oxygen anions as point charges (Burns, 1993).

The parameters of the isothermal EOS are summarized in Table 1 together with the EOS parameters for samples of δ-(Al,Fe)OOH with other compositions that were compressed in helium. The parameters for the crystal-field model are compiled in Table 2. As can be seen in Figure 3, the derived isothermal EOS including the excess pressure $P^{\#}(V,T_0)$ describes the experimental pressure–volume data very well. Furthermore, the parameters of the isothermal contribution to the EOS are consistent with the range of previously reported parameters for the EOS of δ-(Al,Fe)OOH (Sano-Furukawa et al., 2009; Ohira et al., 2019; Su, Zhao, Lv, et al., 2021, Table 1). Likewise, the parameters of the electronic contribution to the EOS are similar to those for Fe^{3+} in octahedral coordination in other high-pressure phases if evaluated with the crystal-field model (Buchen, 2021; Criniti et al., 2025, Table 2).

Table 2
Parameters of the Crystal-Field Model for Ferric Iron

Fe^{3+} in	δ-(Al,Fe)OOH	Calcium ferrite-type phase	
	This study	Buchen (2021)	Criniti et al. (2025)
Δ_0 (cm^{-1})	15374(94)	14750[a]	14750[a]
B_0 (cm^{-1})	655[a]	655[a]	651(10)
C/B	4.73[a]	4.73[a]	4.73[a]
δ	5[a]	5[a]	5.1(3)
b (= c)	−0.94(12)	−2.0(3)	−2

Note. Values without uncertainties in parentheses were fixed. [a]Values from Burns (1993).

3.3. Phonon Density of States of δ-(Al,Fe)OOH at High Pressures

Figure 4 shows the projected partial phonon densities of states (p^3DOS) of ^{57}Fe atoms in δ-(Al,Fe)OOH with Fe/(Al+Fe) = 0.13 together with previously reported p^3DOS for δ-(Al,Fe)OOH with Fe/(Al+Fe) = 0.12 (Ohira et al., 2021). Within their uncertainties, the compositions of the sample used by Ohira et al. (2021) and the sample used in this study are identical. We will therefore discuss and analyze the pressure evolution of the p^3DOS of both samples together. With increasing pressure, the prominent peak at energies between 20 and 30 meV shifts to higher energies while, at the same time, the high-energy tail of this peak gradually gains intensity. At pressures around the spin transition (~40 GPa; Ohira et al., 2019), the p^3DOS changes more fundamentally as the main peak shifts abruptly to higher energies and broadens significantly. Similarly, other parts of the p^3DOS are affected by the spin transition. At pressures above the spin transition, the vibrational energies return to follow a gradual shift to higher energies with increasing pressure.

The spin transition has a clear and distinct effect on the energies of lattice vibrations in δ-(Al,Fe)OOH as expressed in the p^3DOS. The distinct change of vibrational energies across the spin transition likely results from a combination of the concomitant volume change and changes in the strengths of Fe–O bonds. The broadening of the peak in the p^3DOS and the extended spread in vibrational energies with increasing pressure, in turn, reflects a stronger dispersion of vibrational modes with increasing pressure. We note that changes in the vibrational structure caused by the spin transition of Fe^{3+} cations will be amplified in the

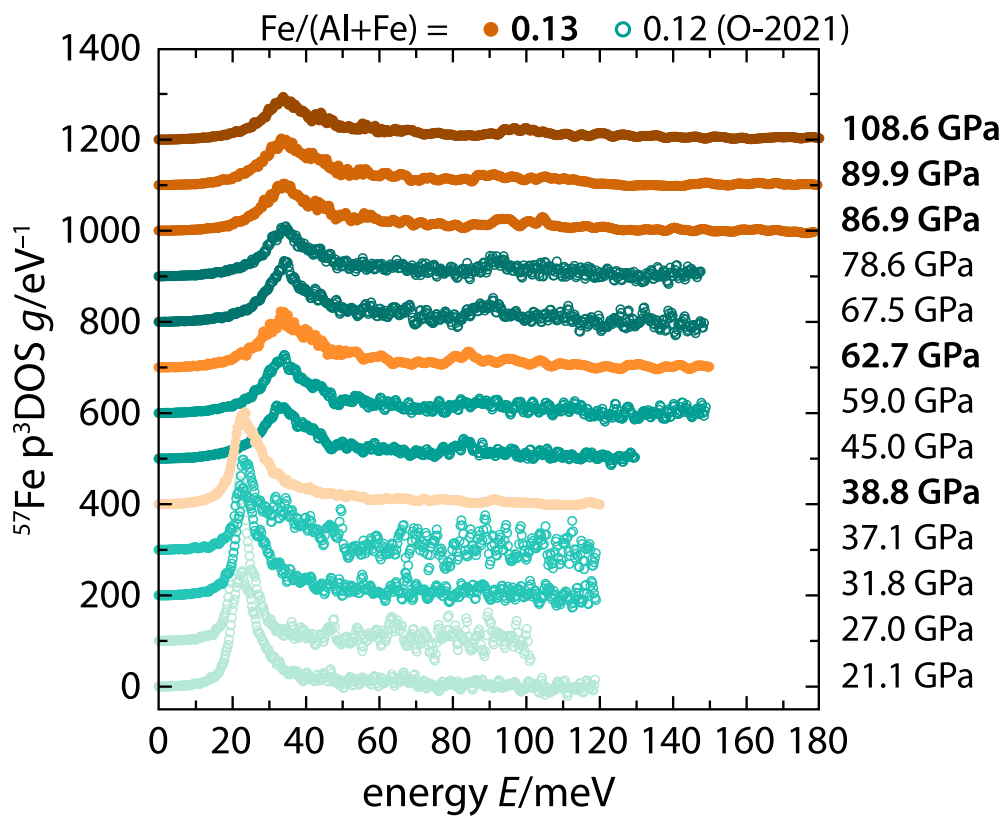

Figure 4. Projected partial phonon densities of states (p^3DOS) of ^{57}Fe atoms in δ-(Al,Fe)OOH at room temperature derived from NRIXS spectra. p^3DOS are vertically offset for clarity with the respective experimental pressures indicated on the right. Data shown with solid circles in orange colors are from this study. Data shown with open circles in green colors (O-2021) are from Ohira et al. (2021).

p^3DOS as NRIXS selectively samples the vibrational motions of ^{57}Fe atoms. The Fe-selective character of NRIXS is therefore beneficial for resolving and quantifying changes in the spectrum of lattice vibrations caused by a spin transition of Fe atoms.

Qualitatively, the pressure evolution of the p^3DOS of δ-(Al,Fe)OOH is similar to the pressure evolution of the p^3DOS of other Fe-bearing high-pressure phases that are affected by spin transitions, including ferropericlase (Chen et al., 2012; Lin et al., 2006; Yang et al., 2019) and bridgmanite (Wang et al., 2021; Yang et al., 2019). The p^3DOS of δ-(Al,Fe)OOH shown in Figure 4, however, have a higher pressure resolution than previously reported high-pressure p^3DOS data sets derived from NRIXS experiments and are therefore ideally suited for a more quantitative analysis of how the spin transition affects the vibrational energy of a material.

3.4. Vibrational Energies of Iron Atoms in δ-(Al,Fe)OOH

Here, we will evaluate the effect of the spin transition on the vibrational energies E in terms of the mean kinetic energies E_{KIN} per ^{57}Fe atom that may be calculated from the experimental p^3DOS $g(E)$ as (Kohn & Chumakov, 2000):

$$E_{\mathrm{KIN}} = \frac{1}{2}\int_0^{\infty} g(E)E\left[\frac{1}{e^{E/kT}-1}+\frac{1}{2}\right]\mathrm{d}E. \tag{10}$$

For a given p^3DOS, the mean kinetic energy E_{KIN} may be calculated for any temperature. The population factor in brackets in Equation 10 acts to increase the contribution of high-energy vibrations to the mean kinetic energy with increasing temperature. To adequately sample the entire energy range of each p^3DOS including the high-energy portions, we calculated mean kinetic energies over a range of simulated temperatures with $0 < T^* < 3300$ K from each p^3DOS in Figure 4, including the p^3DOS reported by Ohira et al. (2021). The resulting collection of mean kinetic energies is plotted as a function of unit cell volume in Figure 5. Unit cell volumes were obtained from the pressures of NRIXS experiments using the derived isothermal EOS of δ-(Al,Fe)OOH with Fe/(Al+Fe) = 0.13 (Equation 8, Tables 1 and 2).

Although the p^3DOS provides the most complete description of the vibrational energies in terms of the experimental data collected in this study, a more compact description is needed to evaluate the effect of the spin transition on the vibrational energy and on related properties such as thermal pressure, heat capacity, and thermal expansion. Therefore, we approximate the mean kinetic energies derived from the p^3DOS by the kinetic energy of a Debye model:

$$E_{\mathrm{KIN}} = \frac{3}{2}kT\left(\frac{T}{\theta}\right)^3\int_0^{\theta/T}\frac{\tau^3}{e^{\tau}-1}\mathrm{d}\tau. \tag{11}$$

To account for the effect of the spin transition on the mean kinetic energy, we assign an individual Debye temperature θ_i to each electronic state i of Fe atoms and an additional Debye temperature θ_δ to the remainder of the crystal structure. In Appendix A, we show that the overall Debye temperature θ may be calculated from the harmonic mean of the cubed individual Debye temperatures weighted by their atomic fractions a_j as:

$$\frac{1}{\theta^3} = \frac{1-a_{\mathrm{Fe}}}{\theta_\delta^3} + a_{\mathrm{Fe}}\sum_i \frac{\phi_i}{\theta_i^3}. \tag{12}$$

The atomic fraction of iron atoms in a given electronic state i is equal to the product $a_{\mathrm{Fe}}\phi_i$. The fractions $\phi_i(V,T)$ at a given combination of volume and temperature follow from the crystal-field model (see Section 3.1). Following Stixrude and Lithgow-Bertelloni (2005), the individual Debye temperatures $\theta_i(V)$ and $\theta_\delta(\mathrm{V})$ are functions of volume V or finite strain f (Equation 9):

$$\theta_i^2 = \theta_{i0}^2\left[1+6\gamma_{i0}f+\frac{1}{2}\left(36\gamma_{i0}^2-12\gamma_{i0}-18q_{i0}\gamma_{i0}\right)f^2\right] \tag{13}$$

with the parameters θ_{i0}, γ_{i0}, and q_{i0}.

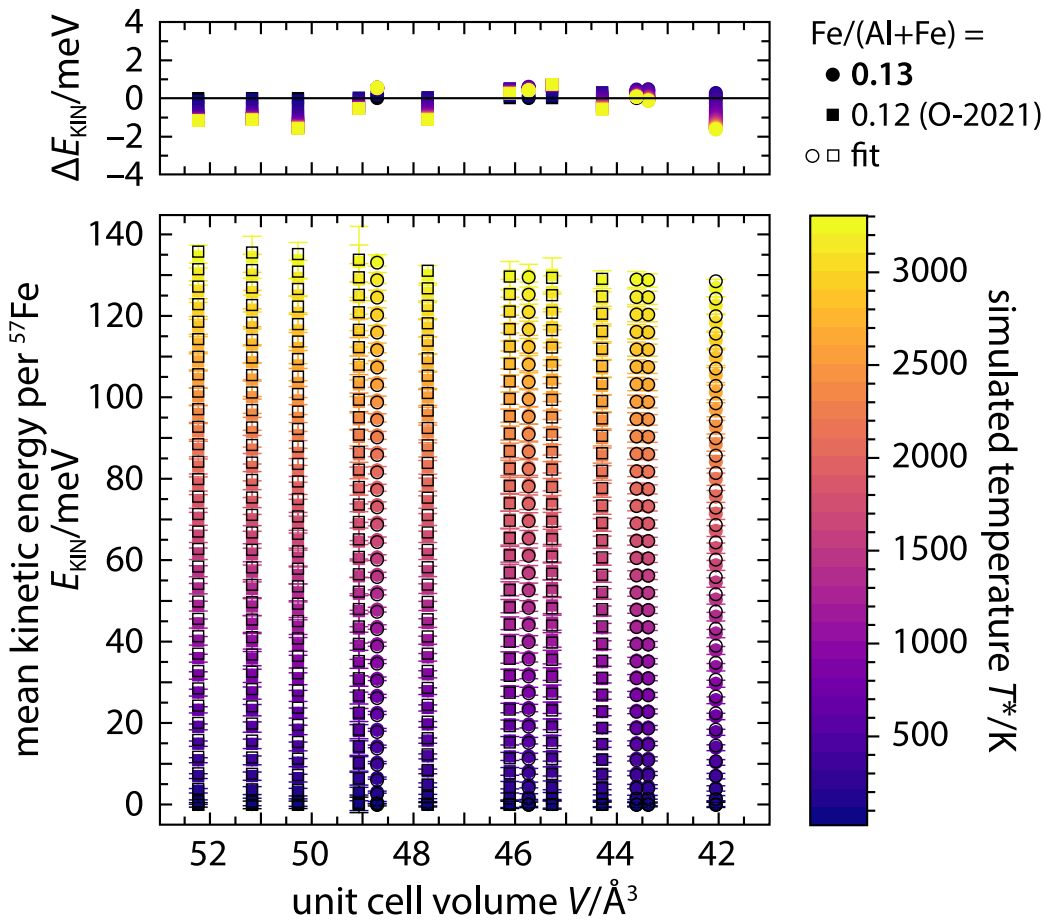

Figure 5. Mean kinetic energies of ^{57}Fe atoms in δ-(Al,Fe)OOH calculated directly from the p^{3}DOS in Figure 4 and for a range of simulated temperatures T^* (colored symbols). The mean kinetic energies were fit to a multi-state Debye model that accounts for changes in the vibrational energies caused by the spin transition of ferric iron (open squares and circles). The top panel shows fitting residuals. Error bars arise from propagating the uncertainties on the p^{3}DOS. Mean kinetic energies shown with squares (O-2021) were calculated from the p^{3}DOS of Ohira et al. (2021).

To constrain the parameters θ_{i0}, γ_{i0}, and q_{i0} of the high-spin $\left({}^6A_1\right)$ and low-spin $\left({}^2T_2\right)$ states, we fit Equation 11 to the mean kinetic energies derived from the p^{3}DOS (Figure 5). For this fit, we set $a_{\mathrm{Fe}} = 1$ in Equation 12 because only vibrations of Fe atoms contribute to the p^{3}DOS. At room temperature, the third state with intermediate spin $\left({}^4T_1\right)$ is not sufficiently populated to contribute significantly to the p^{3}DOS. As a result, the mean kinetic energies derived from the p^{3}DOS may not be used to constrain the parameters θ_{i0}, γ_{i0}, and q_{i0} for this state. Instead, we approximated their values with the respective averages of the high-spin and low-spin states.

At pressures between 10 and 20 GPa, members of the δ-(Al,Fe)OOH solid solution go through a phase transition with an associated change in space group symmetry from $P2_1nm$ at low pressure to $Pnnm$ at high pressure (Gleason et al., 2013; Ohira et al., 2019; Sano-Furukawa et al., 2009, 2018; Satta et al., 2024; Thompson et al., 2020). This phase transition limits the pressure interval over which the high-spin state dominates the p^{3}DOS of δ-(Al,Fe)OOH with space group symmetry $Pnnm$ (Ohira et al., 2021). As a consequence, we had to fix some of the parameters during fitting and found that $\gamma_{i0} = 1$ and $q_{i0} = 0.5$ resulted in reasonable values for the Debye temperatures with $\theta_0\left({}^6A_1\right) = 354(3)$ K and $\theta_0\left({}^2T_2\right) = 648(3)$ K. Our model captures the changes in mean kinetic energies of Fe atoms across the spin transition as evidenced by the low fitting residuals in Figure 5.

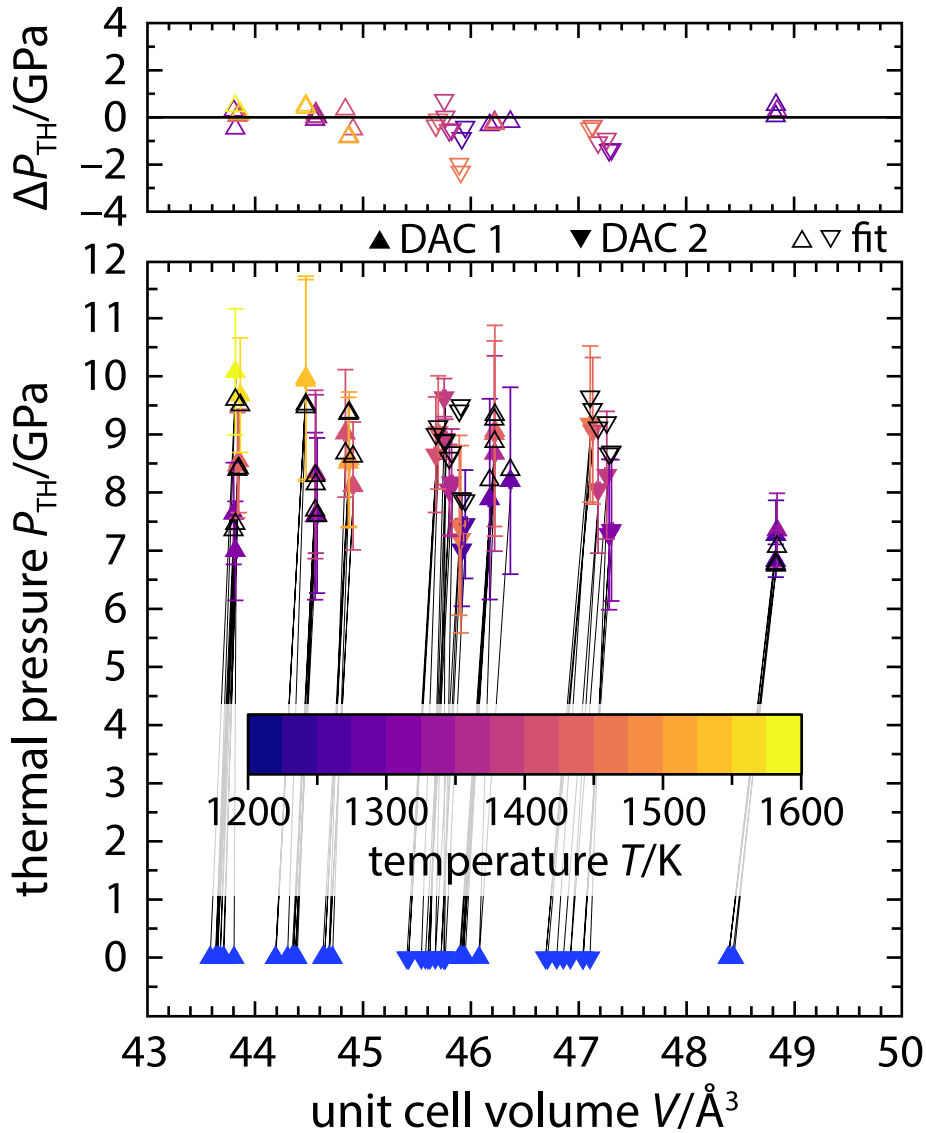

Figure 6. Thermal pressures for δ-($Al_{0.87}$ $Fe_{0.13}$)OOH. The thermal pressures were fit to an equation of state that accounts for excess contributions to pressure due to the spin transition of ferric iron. Tie lines connect data points of laser-heating cycles with room-temperature data shown in blue. The top panel shows fitting residuals. Error bars include propagated contributions from experimental uncertainties on volumes and temperatures.

3.5. Thermal Equation of State of δ-(Al,Fe)OOH

NRIXS selectively samples the vibrations of ^{57}Fe atoms and is therefore ideally suited for detecting and quantifying changes in the vibrational structure across spin transitions of Fe. The vibrations of ^{57}Fe atoms, however, constitute only a subset of all lattice vibrations that contribute to the overall vibrational energy of δ-(Al,Fe)OOH. In the definition of the overall Debye temperature θ (Equation 12), the contribution of vibrations other than those of Fe atoms is captured by the Debye temperature θ_δ. The thermal pressures P_{TH} derived from our high-pressure high-temperature XRD experiments (Section 2.3, Figure 6) include vibrational contributions from all atoms in the crystal structure and may therefore be used to constrain the parameters $\theta_{\delta 0}$, $\gamma_{\delta 0}$, and $q_{\delta 0}$ for the Debye temperature θ_δ.

According to the Mie–Grüneisen EOS, the vibrational contribution $P_{VIB}(V,T)$ to thermal pressure can be calculated from the change in vibrational energy $\Delta U_{VIB}(V,T) = U_{VIB}(V,T) - U_{VIB}(V,T_0)$ as:

Table 3
Thermal Parameters of δ-$Al_{0.87}$ $Fe_{0.13}$OOH

	$^6A_1$	$^2T_2$	$^4T_1$	δ
θ_0 (K)	354(3)	648(3)	501(3)[a]	492(144)
γ_0	1	1	1	0.85(4)
q_0	0.5	0.5	0.5	0.5

Note. Values without uncertainties in parentheses were fixed. [a]Average of $^6A_1$ and $^2T_2$.

$$P_{\mathrm{VIB}}(V,T) = \frac{\gamma}{V}\Delta U_{\mathrm{VIB}}(V,T) \tag{14}$$

where $\gamma = -\partial \ln\theta/\partial \ln V$ is the Grüneisen parameter. $\Delta U_{\mathrm{VIB}}(V,T)$ is calculated from a Debye model (Ita & Stixrude, 1992; Stixrude & Lithgow-Bertelloni, 2005) for which we use the overall Debye temperature θ as defined in Equation 12. The total thermal pressure is the sum of the vibrational contribution $P_{\mathrm{VIB}}(V,T)$ and an excess contribution due to the spin transition:

$$P_{\mathrm{TH}}(V,T) = P_{\mathrm{VIB}}(V,T) + P^{\#}(V,T) - P^{\#}(V,T_0). \tag{15}$$

The excess contributions $P^{\#}(V,T)$ and $P^{\#}(V,T_0)$ can be calculated from the crystal-field model (Section 3.1). We fit Equation 15 to the experimentally observed thermal pressures and obtained the values $\theta_{\delta 0} = 492(144)$ K and $\gamma_{\delta 0} = 0.85(4)$ when setting $q_{\delta 0} = 0.5$. All other parameters were fixed during fitting. With very few exceptions, the resulting thermal EOS for δ-(Al,Fe)OOH matches the experimentally observed thermal pressures within their uncertainties (Figure 6). All parameters of the thermal EOS are collected in Table 3.

4. Thermodynamic Excess Contributions

The effect of the spin transition of ferric iron on the thermodynamic properties and potentials of δ-(Al,Fe)OOH may be evaluated in terms of excess contributions. The excess contributions are the changes in properties that arise from the spin transition. As a central advantage over other EOS formulations for spin transitions, the combination of the crystal-field model with a multi-state Debye model allows to directly access excess contributions to the Helmholtz free energy and the vibrational energy as well as to any properties derived from these energy terms. For a given property A, the excess contribution is equal to the difference $\Delta^{\#}A = A^{\#} - A$ where $A^{\#}$ is the value of the property that includes the effect of the spin transition whereas the value A does not. With our model for the effects of the spin transition on the Helmholtz free energy (Equation 5) and the Debye temperature (Equation 12), we obtain the value $A^{\#}$ by letting the fractions ϕ_i of Fe^{3+} cations with the electronic configurations $^6A_1$ (high spin), $^2T_2$ (low spin), and $^4T_1$ (intermediate spin) vary with pressure and temperature as dictated by our crystal-field model. To obtain the value A, in turn, we set all $\phi_i = \phi_{i0}$ at any combination of pressure and temperature, that is, $\phi(^6A_1) = 1$ and $\phi(^2T_2) = \phi(^4T_1) = 0$.

The variation of the fractions ϕ_i as predicted by our description of the spin transition is plotted in Figure 7a for an isothermal compression path at 298 K and an adiabatic compression path starting at 25 GPa and 1900 K. The adiabatic compression path was calculated for a pyrolitic bulk composition (Buchen, 2021) and is regarded here as a proxy for the average temperature of the ambient lower mantle. Figure 7a shows the typical cross-over of the fractions of the high-spin $(^6A_1)$ and low-spin $(^2T_2)$ states with increasing pressure. At temperatures of the lower mantle, the pressure interval over which both states are populated with significant fractions of Fe^{3+} cations broadens substantially. The state $^4T_1$ with intermediate spin is barely occupied at room temperature. At temperatures of the lower mantle, however, the electronic configuration of more than 20% of the iron atoms corresponds to this state according to our crystal-field model. Because the fraction $\phi(^4T_1)$ of cations in the state $^4T_1$ varies much less with pressure than the fractions of cations in the high-spin $(^6A_1)$ and low-spin $(^2T_2)$ states, the main consequence of including a third state with intermediate spin is to attenuate the effect on physical properties when the majority of Fe^{3+} cations transitions from the high-spin to the low-spin state. The populations of states with intermediate spins, however, have often been ignored in previous descriptions of spin transitions.

To illustrate the excess contributions that arise from the spin transition of Fe^{3+} in δ-(Al,Fe)OOH, Figure 7b shows the evolution of selected thermodynamic properties with pressure along an isothermal compression path at 298 K. Each property has been calculated by including and excluding the effect of the spin transition to illustrate the impact on the respective property. The difference between both cases is equal to the excess contribution to the respective property. The spin transition has a distinct effect on all depicted properties. The Debye temperature θ, for instance, shows an additional increase at pressures between 30 and 40 GPa. As a consequence, the Grüneisen parameter γ shows a peak that is centered on the same pressure interval. Likewise, the spin transition causes positive excursions of the coefficient of thermal expansion α and the isobaric heat capacity C_P towards higher

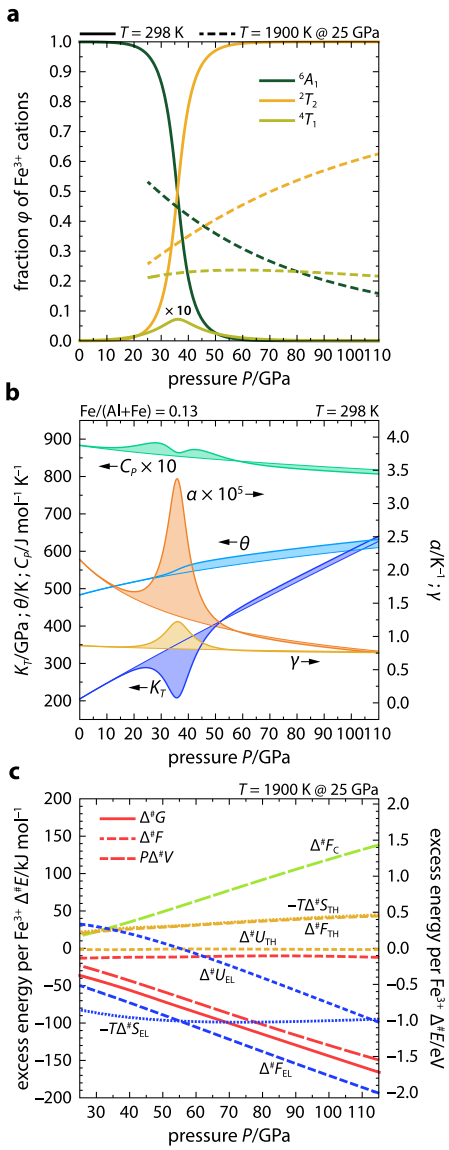

Figure 7. Effect of the spin transition of ferric iron on thermodynamic properties of δ-(Al,Fe)OOH. (a) Relative populations of electronic states of ferric iron as a function of pressure for isothermal compression at 298 K (solid lines) and along an adiabatic temperature profile starting at 1900 K and 25 GPa (dashed lines). (b) Physical properties of δ-($Al_{0.87}$ $Fe_{0.13}$)OOH as a function of pressure for isothermal compression at 298 K. K_T: isothermal bulk modulus, θ: Debye temperature, C_P: molar isobaric heat capacity, α: coefficient of thermal expansion, γ: Grüneisen parameter. The properties have been calculated by including (bold lines) and excluding (thin lines) the effect of the spin transition. The excess contribution to each property is indicated by the colored shading. Small arrows indicate the respective axis. (c) Excess energy contributions per ferric iron cation along an adiabatic temperature profile starting at 1900 K and 25 GPa. Subscripts identify excess contributions to the cold (C), thermal (TH), and electronic (EL) parts of the Helmholtz free energy F, the internal energy U, and the entropy S. Excess contributions without subscripts refer to total contributions to the Gibbs free energy G, the Helmholtz free energy F, and volume work $P\Delta V$.

values while the isothermal bulk modulus K_T shows the characteristic reduction over the pressure interval of the spin transition. Similar effects on thermodynamic properties have been predicted for spin transitions in other mantle minerals (Wentzcovitch et al., 2009; Z. Wu et al., 2009) and observed for the bulk modulus of other compositions of the phase H solid solution (Ohira et al., 2019; Strozewski et al., 2023).

More relevant to phase equilibria in the Earth's lower mantle, however, are the excess contributions of the spin transition to thermodynamic potentials such as the Helmholtz and Gibbs free energies. Figure 7c shows the excess contributions to the Helmholtz and Gibbs free energies as well as their components in terms of entropy S, internal energy U, and volume work $P\Delta V$ along an adiabatic temperature profile starting at 1900 K and 25 GPa. At pressures above 25 GPa, the excess Gibbs free energy $\Delta^{\#}G$ is negative and decreases further with increasing pressure. The negative excess Gibbs free energy indicates that the spin transition of Fe^{3+} reduces the overall Gibbs free energy of the compound δ-(Al,Fe)OOH at pressures and temperatures of the lower mantle. Furthermore, since $\Delta^{\#}G = \Delta^{\#}F + P\Delta^{\#}V$, Figure 7c shows that the excess Gibbs free energy is dominated by the excess volume work $P\Delta^{\#}V$. This observation emphasizes the importance of pressure–volume data when characterizing spin transitions.

Compositional variations in δ-(Al,Fe)OOH and phase H may affect the pressure interval of the spin transition, both in terms of the pressure at which the populations of high-spin and low-spin states cross over and the width of the transition (Gleason et al., 2013; Nishi et al., 2019; Ohira et al., 2019; Strozewski et al., 2023; Su, Zhao, Xu, et al., 2021). As a consequence, the state populations and excess properties shown in Figure 7 may vary with composition as well. The results of experimental studies that directly probed the populations of electronic states of Fe^{3+} in δ-(Al,Fe)OOH and phase H by means of synchrotron Mössbauer spectroscopy or X-ray emission spectroscopy indicate fairly consistent transition intervals at pressures between 30 and 50 GPa for compositions with up to 0.15 Fe^{3+} cations per formula unit (Ohira et al., 2019; Strozewski et al., 2023; Su, Zhao, Xu, et al., 2021). The transition interval predicted by our model for the spin transition of Fe^{3+} in δ-(Al,Fe)OOH is fully consistent with this pressure range. The excess contributions predicted by our model may therefore be seen as representative for the compositions that have been studied so far. However, further measurements on more complex Fe^{3+}-bearing compositions of the phase H solid solutions are needed to constrain the effect of compositional variations on the spin transitions and the related excess contributions to thermodynamic properties.

The magnitudes of the excess contributions to energy terms as obtained from our model for the spin transition of Fe^{3+} in δ-(Al,Fe)OOH vary between 0 and ±2 eV per Fe^{3+} cation. The order of magnitude of these excess contributions is comparable to the energy differences between individual electronic states derived from first-principles calculations on spin transitions of Fe^{3+} in other materials (Hsu, 2017; Hsu et al., 2011, 2012). A detailed comparison, however, is complicated by different choices of reference energies and the fact that previous studies presented enthalpies of individual electronic states but not excess contributions. The comparison nevertheless

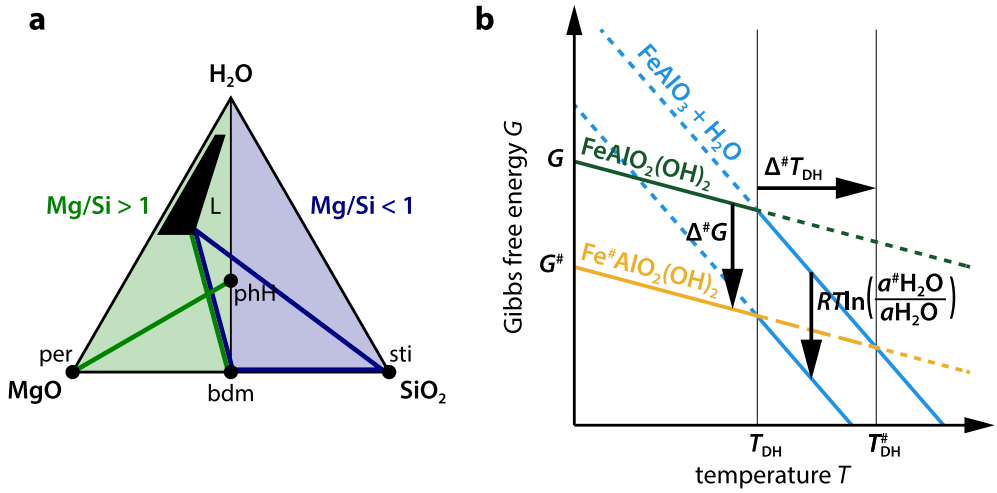

Figure 8. Dehydration reactions of phase H. (a) Ternary diagram showing the compositions of phase H (phH), bridgmanite (bdm), periclase (per), stishovite (sti), and hydrous melt (L) in the system $MgO–SiO_2–H_2O$. The compositional field of the hydrous melt is based on the experimental results of Ghosh and Schmidt (2014). Color shadings and bold colored lines indicate ultramafic (green, Mg/Si > 1) and mafic (blue, Mg/Si < 1) compositions and the respective dehydration reactions of phase H. (b) Schematic illustration of the effect of the spin transition on the dehydration reaction $FeAlO_2(OH)_2 = FeAlO_3 + H_2O$. A reduction in Gibbs free energy by $\Delta^\# G$ due to the spin transition of Fe^{3+} in $FeAlO_2(OH)_2$ may be compensated by reducing the water activity from aH_2O to $a^\#H_2O$ or by raising the dehydration temperature T_{DH} by $\Delta^\# T_{DH}$.

confirms that our model for the spin transition produces realistic excess energies. In the following, we will explore how the excess Gibbs free energy of the spin transition affects phase equilibria in the lower mantle that involve δ-(Al,Fe)OOH as a component of the phase H solid solution.

5. Effect of the Spin Transition on Phase Equilibria of Phase H

In the following, we apply our thermodynamic model to explore the impact of the spin transition of Fe^{3+} in the phase H solid solution on relevant phase equilibria in the lower mantle. More specifically, we will assess the effects of the spin transition on the thermodynamic activity of H_2O in a coexisting hydrous melt and on the dehydration temperature of the phase H solid solution. In experiments at pressures and temperatures of the lower mantle, phase H solid solutions (phH) with different compositions were observed to coexist with hydrous melts (L) and different combinations of the phases bridgmanite (bdm), (ferro)periclase (per), and stishovite (sti) (Ishii, Ohtani, & Shatskiy, 2022; Nishi et al., 2014, 2015; Ohira et al., 2014; Walter et al., 2015; Yuan et al., 2019). These phases are projected into the ternary diagram $MgO–SiO_2–H_2O$ in Figure 8a. The compositional field of the hydrous melt approximates the melt compositions observed in experiments at up to 24 GPa (Ghosh & Schmidt, 2014).

We emphasize that we consider both phase H and a hydrous melt to be minor phases when analyzing the effect of the spin transition on phase equilibria in lower-mantle rocks. This assumption is in accordance with the presumably low H_2O contents of rocks in the lower mantle (Hirschmann, 2006; Ohtani, 2021). Furthermore, we assume that ferric iron is primarily incorporated into phase H as the component $FeAlO_2(OH)_2$, which corresponds to δ-(Al,Fe)OOH with Fe/(Al+Fe) = 0.5. We defined the Fe-Al-bearing component $FeAlO_2(OH)_2$ of the phase H solid solution in analogy to the component $FeAlO_3$ of bridgmanite because $FeAlO_3$ is the dominant Fe^{3+}-bearing component for bridgmanite compositions in both mafic and ultramafic rocks in the lower mantle (Frost et al., 2004; Irifune et al., 2010; Ishii, Miyajima, et al., 2022).

The relative locations of the phases in Figure 8a define potential dehydration reactions of phase H in ultramafic compositions (Mg/Si > 1) as well as in mafic compositions (Mg/Si < 1). In ultramafic compositions, that is, in peridotitic rocks, phase H may dehydrate by the reaction:

$$\text{phH} + \text{per} = \text{bdm} + \text{L}. \quad (16)$$

For the Fe-Al components of phase H and bridgmanite, this reaction may be written as:

$$FeAlO_2(OH)_2 + MgO = FeAlO_3 + H_2O(L) + MgO(L). \quad (17)$$

In mafic compositions, that is, in metabasaltic rocks, phase H may instead dehydrate by the reaction:

$$phH = bdm + sti + L. \quad (18)$$

One way to write this reaction in terms of the Fe-Al components of phase H and bridgmanite would be:

$$FeAlO_2(OH)_2 + MgSiO_2(OH)_2 = FeAlO_3 + SiO_2 + 2\,H_2O(L) + MgO(L) \quad (19)$$

For both of these reactions, the dehydration of the phase H component $FeAlO_2(OH)_2$ is controlled by the equilibrium:

$$FeAlO_2(OH)_2 = FeAlO_3 + H_2O. \quad (20)$$

Here, $FeAlO_3$ may be a component either of bridgmanite or the hydrous melt while H_2O is a component of the hydrous melt.

The effect of the spin transition of Fe^{3+} in the component $FeAlO_2(OH)_2$ of the phase H solid solution on the equilibrium (20) is illustrated schematically in Figure 8b. At a given pressure, the reactant and product sides of the reaction are in chemical equilibrium at the dehydration temperature T_{DH}. At this temperature, the Gibbs free energies on both sides of the reaction are equal. At temperatures below the dehydration temperature, the component $FeAlO_2(OH)_2$ forms part of the phase H solid solution. At higher temperatures, however, the component $FeAlO_2(OH)_2$ breaks down to $FeAlO_3$ and H_2O, which dissolve into bridgmanite and a hydrous melt. The effect of the spin transition is to reduce the Gibbs free energy of the component $FeAlO_2(OH)_2$ by an amount equal to the excess Gibbs free energy $\Delta^{\#}G$. In response to this reduced Gibbs free energy of the component $FeAlO_2(OH)_2$, the reaction may return to chemical equilibrium by two mechanisms. The first mechanism involves a reduction of the Gibbs free energy of the product side by an amount equivalent to $\Delta^{\#}G$ whereas the second mechanism implies a shift of the dehydration temperature to a higher temperature $T^{\#}_{DH}$. While we will investigate both mechanisms separately, they may act together in rocks of the lower mantle, depending on the prevailing chemical environment.

5.1. Effect of the Spin Transition on the Activity of H_2O

The partial molar Gibbs free energy, or chemical potential μ, of a component (C) in a solid or liquid solution (sol) is given by:

$$\mu^{C}_{sol} = \mu^{C*}_{sol} + RT \ln a^{C}_{sol} \quad (21)$$

where μ^{C*}_{sol} is the chemical potential of the pure component at the pressure and temperature of interest, a^{C}_{sol} is the activity of the component in the solid or liquid solution, and R is the gas constant. When reaction (20) is in chemical equilibrium, the change in Gibbs free energy $\Delta_R G$ of the reaction is equal to zero:

$$\Delta_R G = \mu^{H2O}_{L} + \mu^{FeAl}_{bdm/L} - \mu^{FeAl}_{phH} = \Delta^{*}_{R}G + RT \ln \frac{a^{H2O}_{L}\, a^{FeAl}_{bdm/L}}{a^{FeAl}_{phH}} = 0. \quad (22)$$

The Fe-Al components of bridgmanite, hydrous melt, and phase H are abbreviated by the superscript FeAl. $\Delta^{*}_{R}G = \mu^{H2O*}_{L} + \mu^{FeAl*}_{bdm/L} - \mu^{FeAl*}_{phH}$ is the difference in Gibbs free energy between the pure components at the pressure and temperature of interest.

For the first mechanism by which the equilibrium (20) may respond to the spin transition of Fe^{3+} in the component $FeAlO_2(OH)_2$ of phase H, the Gibbs free energy of the product side of reaction (20) needs to be reduced by an amount equal to $\Delta^{\#}G$ in order to counterbalance the reduction in Gibbs free energy on the reactant side due to the spin transition. At a fixed pressure and temperature, according to Equation 21, the required

reduction in Gibbs free energy can only be achieved by changing the activities and hence the concentrations of the components $FeAlO_3$ and H_2O in their respective host phases. The compositions of major mineral phases in lower-mantle rocks such as ferropericlase, bridgmanite, and stishovite, however, are primarily controlled and buffered by the respective bulk rock composition. Furthermore, the H_2O concentrations in bridgmanite and stishovite were found to be significantly reduced or even negligible when these minerals coexisted with a phase H solid solution in experiments (Ishii, Ohtani, & Shatskiy, 2022; Ishii et al., 2024). The chemically most flexible phase might therefore be the hydrous melt. While the relative concentrations of the main oxide components in the melt, that is, MgO, SiO_2, CaO, Al_2O_3, FeO, and Fe_2O_3, are likely to be controlled by the compositions of coexisting major minerals and hence again by the bulk rock composition, the concentration of H_2O in the melt might be more adaptable. We will therefore focus on changing the concentration or, more precisely, the activity $aH_2O = a_L^{H2O}$ of H_2O in the melt phase in order to reduce the Gibbs free energy of the product side of reaction (20).

The activity of H_2O is given by Equation 22 as:

$$aH_2O = a_L^{H2O} = \frac{a_{phH}^{FeAl}}{a_{bdm/L}^{FeAl}} \exp\left(-\frac{\Delta_R^* G}{RT}\right). \tag{23}$$

If the Gibbs free energy μ_{phH}^{FeAl*} of the pure component $FeAlO_2(OH)_2$ changes by $\Delta^{\#}G$ as a result of the spin transition, the activity of H_2O in the hydrous melt would need to change by a factor of:

$$\frac{a^{\#}H_2O}{aH_2O} = \frac{a_{phH}^{\#FeAl}}{a_{bdm/L}^{\#FeAl}} \frac{a_{bdm/L}^{FeAl}}{a_{phH}^{FeAl}} \exp\left(\frac{\Delta^{\#}G}{RT}\right). \tag{24}$$

Here, $a^{\#}H_2O$ is the activity of H_2O in the hydrous melt that accounts for the effect of the spin transition of Fe^{3+} in phase H and aH_2O is the activity of H_2O if there was no such spin transition. In the same way, the superscript $^{\#}$ marks the activities of the Fe-Al components of phase H, bridgmanite, and hydrous melt under the action of the spin transition of Fe^{3+} in the component $FeAlO_2(OH)_2$ of phase H. The factor $a^{\#}H_2O/aH_2O$ by which the spin transition changes the activity of H_2O therefore depends both on the excess Gibbs free energy $\Delta^{\#}G$ and on how the activity ratio $a_{phH}^{FeAl}/a_{bdm/L}^{FeAl}$ and hence the partitioning of Fe-Al components between phases is affected by the spin transition. As we will see, however, the exponential term in Equation 24 most likely dominates the factor $a^{\#}H_2O/aH_2O$ even if changes in the activities of the Fe-Al components might modify the exact value to some extent.

The exponential term $\exp[\Delta^{\#}G/(RT)]$ is plotted in Figure 9 along selected isothermal and adiabatic temperature profiles. For each temperature profile, we calculated the excess Gibbs free energy $\Delta^{\#}G$ per Fe^{3+} cation from our model for the spin transition of Fe^{3+} in δ-(Al,Fe)OOH. In principle, the excess Gibbs free energy per Fe^{3+} cation in δ-(Al,Fe)OOH corresponds to $\Delta^{\#}G$ for the component $FeAlO_2(OH)_2$ of the phase H solid solution. As mentioned in Section 4, however, the thermodynamic excess contributions may vary with composition, for example, if some characteristics of the spin transition change in compositions that include the phase H component $MgSiO_2(OH)_2$ (Strozewski et al., 2023). Following the here-presented formalism to evaluate thermodynamic excess contributions that arise from the spin transition of Fe^{3+} in δ-(Al,Fe)OOH, future studies may extend the model to include the effects of compositional variations within the phase H solid solution.

Along all selected temperature profiles in Figure 9, the term $\exp[\Delta^{\#}G/(RT)]$ decreases with increasing pressure by several orders of magnitude. The reduction is more pronounced for colder temperature profiles than for hotter profiles but remains significant even at realistic temperatures of the lower mantle. The adiabatic temperature profile starting at 1900 K at 25 GPa, for example, has been calculated for a pyrolitic bulk composition (Buchen, 2021) and closely resembles other estimates for the adiabatic temperature profile of the ambient lower mantle (Katsura, 2022). Even along this relatively hot temperature profile, the term $\exp[\Delta^{\#}G/(RT)]$ decreases by a factor of 0.007 from 25 to 100 GPa. Colder adiabatic temperature profiles that extrapolate the temperatures of subduction zones into the lower mantle lead to more extreme reductions of the term $\exp[\Delta^{\#}G/(RT)]$.

At pressures that correspond to a depth of about 1,000 km, the values of $\exp[\Delta^{\#}G/(RT)]$ appear to be virtually independent of the temperatures of adiabatic temperature profiles at this depth. Deeper in the lower mantle, lower

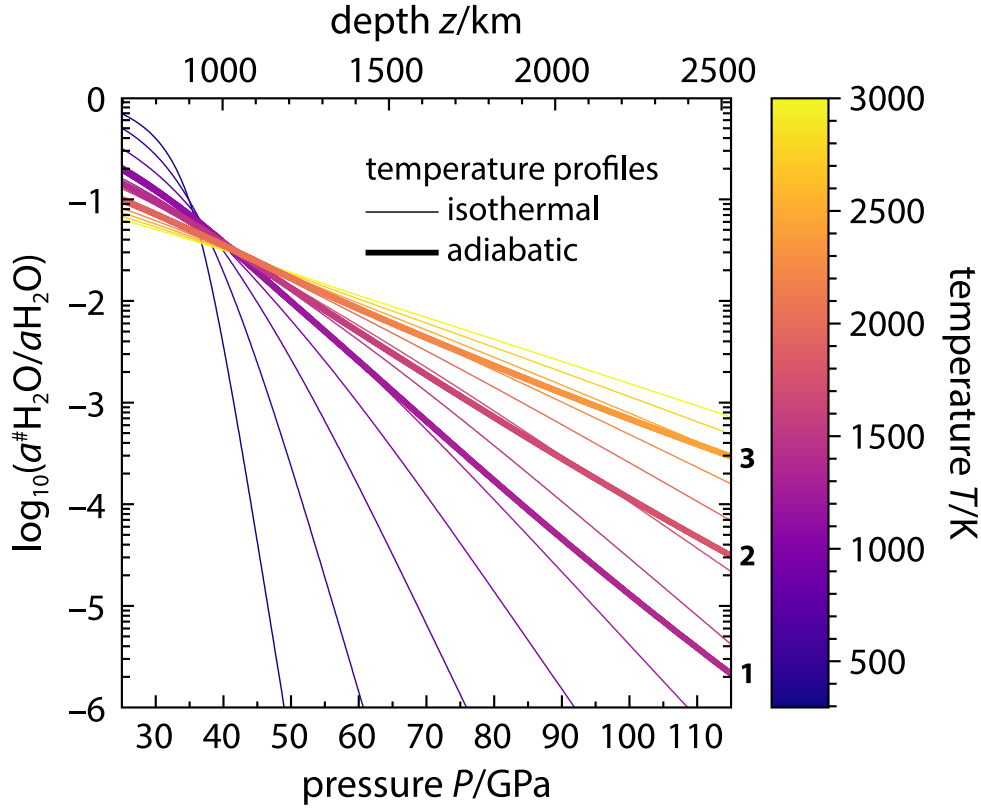

Figure 9. Effect of the spin transition of Fe^{3+} in phase H on the activity of H_2O as expressed by the factor $a^{\#}H_2O/aH_2O$. The factor $a^{\#}H_2O/aH_2O$ was approximated by the term $\exp[\Delta^{\#}G/(RT)]$ and calculated along selected isothermal and adiabatic temperature profiles. The adiabatic temperature profiles marked 1, 2, and 3 start at 25 GPa and 1100, 1400, and 1900 K, respectively (see also Figure 10).

temperatures imply smaller values of $\exp[\Delta^{\#}G/(RT)]$ while the effect of temperature is reversed and generally weaker at depths shallower than 1,000 km. This implies that the effect of the spin transition of Fe^{3+} in phase H on the activity of H_2O is strongest and more sensitive to temperature in deeper parts of the lower mantle. In the shallow lower mantle, the effect is weaker and significantly less sensitive to temperature as reflected by the clustering of the curves for $\exp[\Delta^{\#}G/(RT)]$ at depths shallower than 1,000 km (Figure 9).

As mentioned above, changes in the activities of the Fe-Al components of bridgmanite, hydrous melt, and phase H may partially compensate for the effect of the exponential term $\exp[\Delta^{\#}G/(RT)]$ on the ratio $a^{\#}H_2O/aH_2O$ in Equation 24. Although the exact activity–composition relations for the Fe-Al components of these phases are not known, changing their activity ratio by a factor that fully offsets the reduction of the exponential term $\exp[\Delta^{\#}G/(RT)]$ would either require fairly extreme changes in the activity–composition relations or an inversion of the partitioning behavior of the Fe-Al components. Certainly, the spin transition of Fe^{3+} in the component $FeAlO_2(OH)_2$ may alter the activity–composition relation for this component and modify the partitioning of Fe^{3+} between phase H and bridgmanite and between phase H and a hydrous melt. Changes in the activity ratio $a_{phH}^{FeAl}/a_{bdm/L}^{FeAl}$ of several orders of magnitude, however, appear less realistic.

In bulk rock compositions with low overall H_2O contents, for instance, there will not be enough H_2O available to form a sufficiently large amount of the component $FeAlO_2(OH)_2$ by extracting the component $FeAlO_3$ from bridgmanite in order to significantly change the concentration and hence the activity of this component in bridgmanite. In such a case, the activity of the $FeAlO_3$ component in bridgmanite would remain almost unchanged and primarily controlled by the bulk rock composition and by the partitioning of elements between the major rock-forming minerals. Fully compensating for the reduction of the term $\exp[\Delta^{\#}G/(RT)]$ would then require changing the activity a_{phH}^{FeAl} of the component $FeAlO_2(OH)_2$ in phase H by a factor of $\exp[-\Delta^{\#}G/(RT)]$ in response to the spin

transition. Again, such extreme changes in the activity of the component $FeAlO_2(OH)_2$ appear unrealistic. We therefore conclude that the exponential term $\exp[\Delta^{\#}G/(RT)]$ likely dominates the factor $a^{\#}H_2O/aH_2O$, at least, along colder temperature profiles and if mineral compositions are buffered by the bulk rock composition.

5.2. Effect of the Spin Transition on the Dehydration Temperature

The second mechanism by which the equilibrium (20) may respond to the spin transition of Fe^{3+} in the component $FeAlO_2(OH)_2$ of phase H consists in a shift of the equilibrium or dehydration temperature T_{DH} to a higher temperature $T^{\#}_{DH}$. This mechanism would become active if the concentrations and hence the activities of all components in reaction (20) remain unchanged, including the activity of H_2O. In a rock of the lower mantle, such a situation may result if the activity of H_2O is buffered at a nearly constant value, for example, by the dehydration of other hydrous phases or by the release of H_2O from hydrated NAMs. At the same time, the activities of the Fe-Al components of bridgmanite, hydrous melt, and phase H should be buffered as well, for example, by the bulk rock composition as explained in the previous section.

Based on an analysis of the relations in Figure 8b and the definition of the entropy $S = -(\partial G/\partial T)_P$, it is possible to derive the following expression for the shift $\Delta^{\#}T_{DH}$ of the dehydration temperature of the component $FeAlO_2(OH)_2$ of phase H:

$$\Delta^{\#}T_{DH} = T^{\#}_{DH} - T_{DH} = -\frac{\Delta^{\#}G}{\Delta_R S} \tag{25}$$

where $\Delta_R S$ is the difference in entropy between the products and reactants of reaction (20):

$$\Delta_R S = S_L^{H2O*} + S_{bdm/L}^{FeAl*} - S_{phH}^{FeAl*} - R \ln \frac{a_L^{H2O} a_{bdm/L}^{FeAl}}{a_{phH}^{FeAl}}. \tag{26}$$

As with the chemical potential, the asterisk $(*)$ marks the properties of pure components.

Both the excess Gibbs free energy $\Delta^{\#}G$ and the entropy S_{phH}^{FeAl*} of the component $FeAlO_2(OH)_2$ of phase H may be calculated from the thermal equation of state and crystal-field model for δ-(Al,Fe)OOH that we derived from our experimental data on δ-(Al,Fe)OOH with Fe/(Al+Fe) = 0.13. All excess contributions to properties that arise from the spin transition were scaled to their values per Fe^{3+} cation to account for the formula of the component $FeAlO_2(OH)_2$. We did not adjust the values of any EOS parameters of the model (Tables 1–3) for the difference in the ratio Fe/(Al+Fe). Once additional data on phase H solid solutions with a pressure resolution comparable to our data becomes available, the variation of model parameters, including the parameters of the EOS and the crystal-field model, with composition may be taken into account as well.

Following the approach of Komabayashi and Omori (2006), we estimated the entropy S_L^{H2O*} of H_2O as a component of a hydrous melt from thermodynamic data on H_2O (Robie et al., 1978). The entropy S_{bdm}^{FeAl*} of the bridgmanite component $FeAlO_3$ may be calculated from tabulated thermodynamic data (Stixrude & Lithgow-Bertelloni, 2024) in combination with a Debye model (Ita & Stixrude, 1992; Stixrude & Lithgow-Bertelloni, 2005). To estimate the entropy S_L^{FeAl*} of the component $FeAlO_3$ in a hydrous melt, we added the entropy of melting reported for $MgSiO_3$ bridgmanite of approximately 60 J mol^{-1} K^{-1} (Deng et al., 2023; Stixrude & Karki, 2005) to the calculated entropy of the bridgmanite component $FeAlO_3$. At relevant combinations of pressures and temperatures, these approximations suggest values of 430 J mol^{-1} K^{-1} $< S_L^{H2O*} + S_{bdm/L}^{FeAl*} <$ 590 J mol^{-1} K^{-1}. In view of the uncertainties on these entropy estimates, however, we decided to vary the entropies $S_L^{H2O*} + S_{bdm/L}^{FeAl*}$ between 300 and 800 J mol^{-1} K^{-1} when evaluating the shift $\Delta^{\#}T_{DH}$. Another source of uncertainty arises from the unknown value of the ratio of activities in Equation 26. Varying the value of the activity ratio by six orders of magnitude, for example, from 0.001 to 1000, translates into a total change of entropy by about 120 J mol^{-1} K^{-1}. We explored the effect of this additional uncertainty on the calculated values of the shift $\Delta^{\#}T_{DH}$ as well.

Apart from very few constraints (Nishi et al., 2015), the dehydration temperatures of Fe-bearing phase H at pressures of the lower mantle remain unknown. To evaluate how the spin transition of Fe^{3+} in phase H affects the

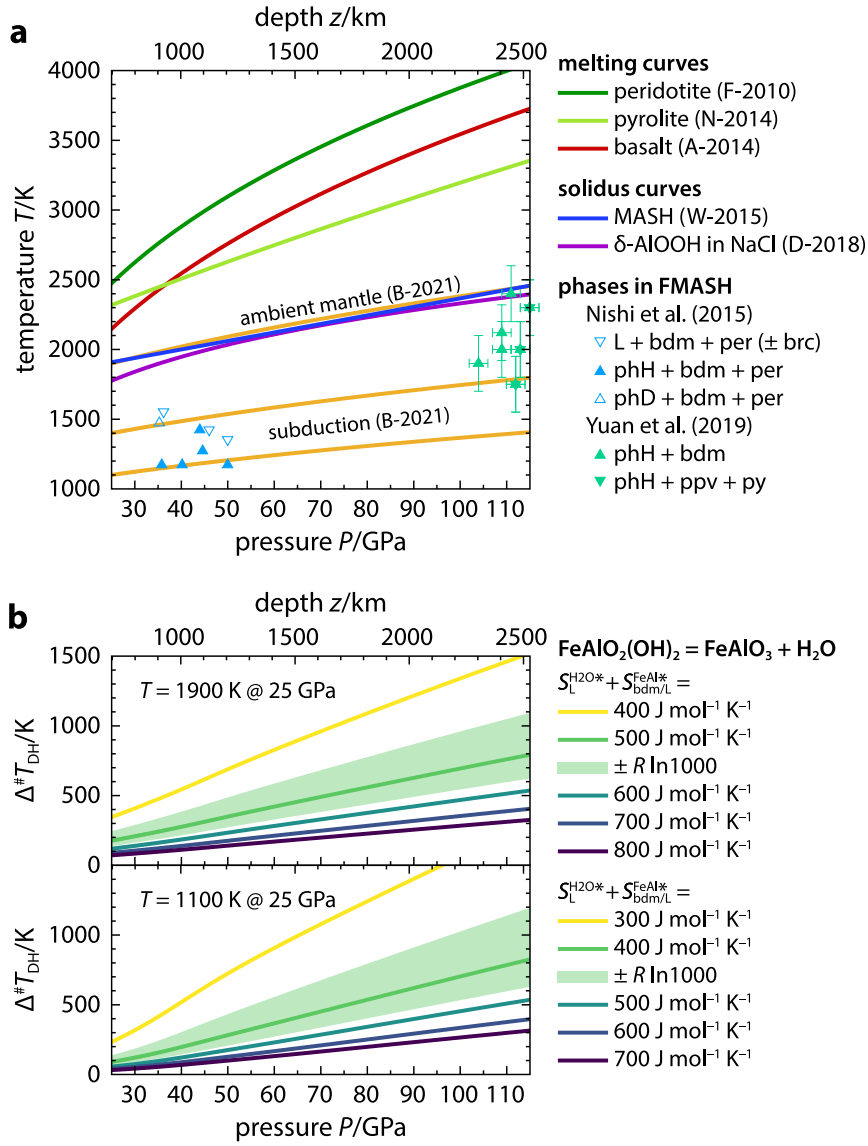

Figure 10. Effect of the spin transition of Fe^{3+} in phase H on the dehydration temperature. (a) Melting curves of lower-mantle rocks and solidus curves for the system $MgO–Al_2O_3–SiO_2–H_2O$ (MASH) and for δ-AlOOH in NaCl. Adiabatic temperature profiles for the ambient mantle and for cold and very cold subduction zones are shown as orange curves. The pressure–temperature combinations for phase assemblages observed in experiments on the system $FeO/Fe_2O_3–MgO–Al_2O_3–SiO_2–H_2O$ (FMASH) are shown with colored symbols. phH: phase H, bdm: bridgmanite, per: (ferro)periclase, L: hydrous melt, brc: brucite, ppv: post-perovskite, py: pyrite-structured phase. References: F-2010: Fiquet et al. (2010), N-2014: Nomura et al. (2014), A-2014: Andrault et al. (2014), W-2015: Walter et al. (2015), D-2018: Duan et al. (2018), B-2021: Buchen (2021). (b) Shifts $\Delta^{\#}T_{DH}$ of the dehydration temperature of the component $FeAlO_2(OH)_2$ of phase H that result from the spin transition of Fe^{3+}. The shifts have been calculated along two adiabatic temperature profiles starting at 1900 and 1100 K at 25 GPa and assuming different entropies of the dehydration products $FeAlO_3$ and H_2O. Adding or subtracting the term R ln 1000 is equivalent to varying the activity ratio in Equation 26 from 0.001 to 1000.

dehydration temperature, we need to calculate the excess Gibbs free energy $\Delta^{\#}G$ and the entropy change $\Delta_R S$ at relevant combinations of pressure and temperature. We therefore chose to calculate the shift $\Delta^{\#}T_{DH}$ of the dehydration temperature of the component $FeAlO_2(OH)_2$ along two adiabatic temperature profiles through the lower mantle. Starting at 25 GPa and 1900 K, the first temperature profile approximates the average temperature of the ambient lower mantle and runs very close to the experimentally observed dehydration curve of δ-AlOOH in NaCl (Duan et al., 2018) and the solidus curve in the system $MgO–SiO_2–Al_2O_3–H_2O$, which at pressures above

50 GPa corresponds to the dehydration curve of Al-bearing phase H (Walter et al., 2015). The second temperature profile starts at 25 GPa and 1100 K and extrapolates the temperatures of a very cold subduction zone into the lower mantle. This second temperature profile runs slightly below the dehydration temperatures reported for Fe-bearing phase H compositions at pressures of up to 50 GPa (Nishi et al., 2015). Both temperature profiles are plotted together with reported melting and solidus curves in Figure 10a.

The calculated shifts $\Delta^{\#}T_{\mathrm{DH}}$ of the dehydration temperature of the component $FeAlO_2(OH)_2$ of phase H that result from the spin transition of Fe^{3+} in this component are shown in Figure 10b. Along both temperature profiles and for all considered estimates of the entropies $S_{\mathrm{L}}^{\mathrm{H2O}*} + S_{\mathrm{bdm/L}}^{\mathrm{FeAl}*}$, the spin transition significantly raises the dehydration temperature of the component $FeAlO_2(OH)_2$. Depending on the exact combination of temperature profile and entropy estimate, the shift $\Delta^{\#}T_{\mathrm{DH}}$ of the dehydration temperature varies from about 30 K at 25 GPa to 1800 K at 115 GPa. For all considered scenarios, the shift $\Delta^{\#}T_{\mathrm{DH}}$ increases with increasing pressure. At 100 GPa, the calculated shifts vary between 260 and 1560 K. Changing the ratio of activities in Equation 26 has a similar effect on the calculated shifts $\Delta^{\#}T_{\mathrm{DH}}$ like changing the entropies $S_{\mathrm{L}}^{\mathrm{H2O}*} + S_{\mathrm{bdm/L}}^{\mathrm{FeAl}*}$. Reducing the activity ratio reduces the magnitude of $\Delta^{\#}T_{\mathrm{DH}}$.

6. Implications for the Stability of Phase H and the Storage of H_2O in the Lower Mantle

The results of our thermodynamic analysis of how the spin transition of Fe^{3+} in phase H affects phase equilibria have implications for the formation and stability of Fe^{3+}-bearing phase H in rocks of the lower mantle. While we formulated our analysis in terms of the Fe-Al components $FeAlO_2(OH)_2$ and $FeAlO_3$ of phase H and bridgmanite or a hydrous melt, respectively, the same analysis may be put forward in terms of other Fe^{3+}-bearing components of these phases. In fact, we normalized all excess properties in our analysis such as the excess Gibbs free energy $\Delta^{\#}G$ that arise from the spin transition of Fe^{3+} in phase H to one Fe^{3+} cation. Within certain limits, the magnitudes of the effects of the spin transition on the activity of H_2O in a coexisting hydrous melt and on the dehydration temperature of phase H may therefore be transferred to other Fe^{3+}-bearing components of phase H by taking into account the number of Fe^{3+} cations per formula unit of the respective component.

The magnitude of the effect of the spin transition of Fe^{3+} in phase H on phase equilibria may be reduced if the equilibrium reaction (20) or an analogous dehydration reaction is affected by a spin transition of Fe^{3+} in a component of the dehydration products, for instance, if the component $FeAlO_3$ of bridgmanite underwent a spin transition. While a spin transition of Fe^{3+} in the component $FeAlO_3$ of bridgmanite is currently not supported by experimental or computational data (Glazyrin et al., 2014; Hsu et al., 2012; Lin et al., 2016), spin transitions of Fe^{3+} have been reported for other Fe^{3+}-bearing components of bridgmanite (Catalli et al., 2010; Hsu et al., 2011; J. Liu et al., 2018) as well as for other anhydrous phases that may contribute to the mineral assemblage of the lower mantle (Criniti et al., 2025; Y. Wu et al., 2016, 2017). If these components are involved in dehydration reactions of phase H, their spin transitions may, to some extent, compensate for the effect of the spin transition of Fe^{3+} in phase H on the respective equilibrium.

As the first central finding, our thermodynamic analysis suggests that the spin transition of Fe^{3+} in phase H may have a strong impact on the activity of H_2O in a coexisting hydrous melt. With increasing pressure, the spin transition causes a reduction of the activity of H_2O by a factor equal to the ratio $a^{\#}H_2O/aH_2O$, which decreases by several orders of magnitude along adiabatic temperature profiles through the lower mantle if approximated by the value of the exponential term $\exp[\Delta^{\#}G/(RT)]$ (Equation 24, Figure 9). A reduction of the H_2O activity by the factor $a^{\#}H_2O/aH_2O$ remains effective even if only a minor amount of Fe^{3+}-bearing phase H or phase H with only a small molar fraction of the component $FeAlO_2(OH)_2$ contributes to the phase assemblage because the chemical potential and hence the activity of H_2O remain buffered by the equilibrium (20) as long as the component $FeAlO_2(OH)_2$ is present. As mentioned above, equilibria involving other Fe^{3+}-bearing components of phase H may have a similar effect on the H_2O activity.

The reduction of the H_2O activity by the spin transition of Fe^{3+} in phase H implies that Fe^{3+}-bearing phase H may form at substantially lower activities and hence concentrations of H_2O in a coexisting melt than without the spin transition. Furthermore, the concentration of H_2O in a hydrous melt that would be needed to crystallize Fe^{3+}-

bearing phase H from the melt decreases with increasing pressure if no other effect counterbalances the reduction in the activity of H_2O. The critical H_2O concentration that is required to stabilize Fe^{3+}-bearing phase H would then be significantly lower in the deep lower mantle than in the shallow lower mantle. The formation of Fe^{3+}-bearing phase H may hence be more favorable in the lowermost mantle than in the shallow lower mantle. As a consequence, Fe^{3+}-bearing phase H may act as a host for H_2O in the lowermost mantle while H_2O might be released from phase H and transferred to other phases in shallower parts of the lower mantle.

While our thermodynamic analysis predicts the relative reduction in H_2O activity caused by the spin transition of Fe^{3+} in phase H, absolute values of the H_2O activity in a coexisting melt phase may be estimated based on an existing thermodynamic model for the system $MgO–SiO_2–H_2O$ (Komabayashi & Omori, 2006). This model suggests H_2O activities in hydrous melt on the order of 0.01 at around 30 GPa and 1300 K and in equilibrium with phase D or superhydrous phase B (Komabayashi & Omori, 2006), that is, at pressures and temperatures slightly below those at which phase H replaces phase D (Nishi et al., 2014; Ohtani et al., 2014). According to our analysis, the spin transition of Fe^{3+} may then reduce the H_2O activity to values as low as 10^{-6} at 100 GPa along cold adiabatic temperature profiles (Figure 9). At such low H_2O activities, the properties and behavior of the melt phase will approach those of an anhydrous melt.

While a comparison of molar fractions and activities can only be approximate, the molar fraction of H_2O in peridotitic source rocks of plume-derived magmas is on the order of 0.002 in terms of oxide components (750 wt-ppm H_2O; Bolfan-Casanova, 2005; Dixon et al., 2002; Hirschmann, 2006) and will hence be much higher in any partial melt formed from such rocks. The H_2O activities in partial melts of peridotitic rocks in the lower mantle therefore likely exceed the H_2O activities required to stabilize Fe^{3+}-bearing phase H in the lower mantle. Once Fe^{3+}-bearing phase H contributes to the mineral assemblage, the equilibrium reaction (20) or an analogous reaction with an Fe^{3+}-bearing component of phase H will buffer the H_2O activities in the melt at very low levels, especially in the deep lower mantle. As a consequence, the melt may eventually crystallize completely to form a mineral assemblage that includes Fe^{3+}-bearing phase H.

Based on the arguments presented above, the H_2O activities of melts in equilibrium with Fe^{3+}-bearing phase H may be even lower than those required to significantly hydrate NAMs of the lower mantle (Bolfan-Casanova et al., 2000, 2002, 2003; Fu et al., 2019; Ishii, Ohtani, & Shatskiy, 2022; Litasov et al., 2003; Z. Liu et al., 2021). In this case, Fe^{3+}-bearing phase H would act as the main host for H_2O in solid phases of the lower mantle even if present only as a minor phase. Ishii, Ohtani, and Shatskiy (2022) and Ishii et al. (2024) found that the H_2O contents of bridgmanite and stishovite, both of which are NAMs of lower-mantle rocks, were significantly reduced when these NAMs were synthesized together with Al-bearing phase H or δ-AlOOH, respectively, and concluded that phase H solid solutions rather than NAMs are the main solid host phases for H_2O in the lower mantle. The spin transition of Fe^{3+} in phase H may further enhance the strong partitioning of H_2O into phase H and dehydrate coexisting NAMs of the lower mantle almost completely.

If the activity of H_2O in a hydrous melt as well as the activities of the Fe^{3+}-bearing components of phase H, bridgmanite, and hydrous melt are buffered at close to constant values, for example, by equilibria that involve major rock-forming minerals, the spin transition of Fe^{3+} in phase H may stabilize phase H to higher temperatures (Figure 10b). Based on our thermodynamic analysis for the endmember $FeAlO_2(OH)_2$ of the phase H solid solution, we estimated that the shift $\Delta^{\#}T_{DH}$ of the dehydration temperature varies from about 100 K at pressures of the shallow lower mantle to more than 300 K at pressures of about 100 GPa but may even exceed 1000 K, depending on the insufficiently constrained entropy of H_2O in hydrous melts at pressures and temperatures of the lower mantle. Even for very high entropies of the dehydration products, however, the shift $\Delta^{\#}T_{DH}$ remains significant and on the order of several hundred kelvins (Figure 10b).

As obtained from our thermodynamic analysis, the shift $\Delta^{\#}T_{DH}$ of the dehydration temperature of phase H induced by the spin transition of Fe^{3+} only includes the effect of the spin transition itself but does not account for the effect of incorporating iron into phase H. In the case of phase D, the effects of aluminum and iron on the stability limit appear to approximately compensate for each other (Ghosh & Schmidt, 2014). In experiments on natural antigorite and chlorite compositions, Nishi et al. (2015) found a small effect of iron on the dehydration temperature of phase H. Their quenched phase H samples, however, contained relatively minor amounts of iron. Whether the net effect of incorporating ferric iron on the dehydration temperatures of phase H is dominated by the

here-proposed effect of the spin transition needs to await direct experimental verification. The remarkable thermal stability of Fe-Al-bearing compositions of phase H at pressures above 100 GPa (Yuan et al., 2019), however, would be consistent with a shift of the stability limit to higher temperatures with increasing pressure as indicated by the results of our thermodynamic analysis (Figure 10).

While our thermodynamic analysis predicts the shift $\Delta^{\#}T_{DH}$ of the dehydration temperature of the component $FeAlO_2(OH)_2$ of phase H caused by the spin transition of Fe^{3+}, our model may not constrain absolute dehydration temperatures. The increasing values of $\Delta^{\#}T_{DH}$ with increasing pressure (Figure 10b), however, indicate that the spin transition may raise the slope of the dehydration curve of Fe^{3+}-bearing phase H. Previously reported dehydration curves of Fe-free compositions of phase H run almost exactly parallel to adiabatic temperature profiles through the lower mantle and are located at temperatures just below the temperature profile for the ambient mantle (Duan et al., 2018; Walter et al., 2015) (Figure 10a). Raising the slope of these dehydration curves would therefore cause the dehydration curves to intersect with adiabatic temperature profiles. The points of intersection would then mark the conditions and depths at which a phase H-bearing mineral assemblage would form a hydrous melt or crystallize from the melt. The effect of the spin transition of Fe^{3+} on the slope of the dehydration curve of phase H may therefore have important consequences for the formation and stability of hydrous melts in the lower mantle.

The full extent of the shift $\Delta^{\#}T_{DH}$ of the dehydration temperature of phase H applies to the component or endmember $FeAlO_2(OH)_2$. As with other reactions of solid solutions, the dehydration temperature T_{DH} will vary as a function of composition. When moving away from the endmember $FeAlO_2(OH)_2$, for example, in a phase diagram that shows the dehydration temperature as a function of composition, the dehydration temperature may increase or decrease, depending on the dehydration temperatures of the other endmembers of the phase H solid solution and the shape of the dehydration curve or surface. The more the composition of phase H approaches the endmember $FeAlO_2(OH)_2$, however, the more will the dehydration temperature be raised by the effect of the spin transition. Because the effect of the spin transition of Fe^{3+} on the dehydration temperature of phase H is largest for Fe^{3+}-rich compositions of phase H, we speculate that Fe-rich, hydrous regions in the lower mantle may stabilize Fe^{3+}-rich phase H to the highest temperatures and hence be preferred locations for storing H_2O in phase H.

7. Conclusions

Based on the pressure–volume data that we obtained from our high-pressure XRD experiments, we derived the isothermal EOS of δ-(Al,Fe)OOH with Fe/(Al+Fe) = 0.13. We described the effect of the spin transition of ferric iron in δ-(Al,Fe)OOH on the compression behavior in terms of a crystal-field model, the parameters of which were constrained by analyzing our pressure–volume data. With these parameters, the crystal-field model predicts the energies and populations of multi-electron states of Fe^{3+} cations in δ-(Al,Fe)OOH at any combination of volume and temperature. The effect of the spin transition of Fe^{3+} on the frequencies of lattice vibrations of δ-(Al,Fe)OOH is captured by changes in the p^3DOS of ^{57}Fe atoms with pressures. We derived the p^3DOS of δ-(Al,Fe)OOH from our high-pressure NRIXS experiments and combined them with a previously reported set of p^3DOS at complementary pressures (Ohira et al., 2021). We then analyzed the collection of p^3DOS to extract the parameters of a multi-state Debye model for the vibrational energy of Fe atoms in δ-(Al,Fe)OOH. The vibrational energy of the remainder of the crystal structure was described by an additional Debye model, the parameters of which were constrained by analyzing the thermal pressures that we derived from our high-pressure high-temperature XRD experiments on δ-(Al,Fe)OOH with Fe/(Al+Fe) = 0.13.

As the combined result of our analysis of experimental data, we obtained a thermal EOS for δ-(Al,Fe)OOH that accounts for the effect of the spin transition of Fe^{3+} on pressure and vibrational energy. The underlying thermodynamic model may further be used to evaluate the excess contributions of the spin transition on thermodynamic properties and potentials. We used this model to calculate the excess Gibbs free energy that arises from the spin transition of Fe^{3+} in the component $FeAlO_2(OH)_2$ of the phase H solid solution at pressures and temperatures of the lower mantle. A thermodynamic analysis of the dehydration reaction $FeAlO_2(OH)_2 = FeAlO_3 + H_2O$ shows that the spin transition of Fe^{3+} in the component $FeAlO_2(OH)_2$ may have a stabilizing effect on this component and hence on Fe^{3+}-bearing phase H in rocks of the lower mantle. The spin transition of Fe^{3+} in phase H reduces the activity of H_2O in a coexisting hydrous melt by several orders of magnitude and may hence stabilize Fe^{3+}-bearing

phase H at significantly lower activities and hence concentrations of H_2O than without a spin transition. Alternatively, if H_2O activities are buffered, the spin transition may raise the dehydration temperature of Fe^{3+}-bearing phase H. The magnitudes of the effects on the activity of H_2O and on the dehydration temperature increase with increasing pressure and hence with depth in the lower mantle.

The stabilizing effect of the spin transition of Fe^{3+} on the component $FeAlO_2(OH)_2$ of phase H or, more generally, on Fe^{3+}-bearing phase H may have important consequences for the storage of H_2O in solid phases of the lower mantle. The strong reduction of the H_2O activities in a coexisting hydrous melt, for example, may promote the crystallization of Fe^{3+}-bearing phase H even from melts with very low H_2O concentrations like those expected for partial melts of typical mantle rocks. The same effect may enhance the preferential partitioning of H_2O from NAMs of the lower mantle into phase H as observed for Fe-free compositions (Ishii, Ohtani, & Shatskiy, 2022; Ishii et al., 2024) and turn phase H into the primary host phase for H_2O in the lower mantle. Since the effects of the spin transition of Fe^{3+} in phase H on the H_2O activity and dehydration temperature become more pronounced with increasing pressure, H_2O may be preferentially stored in phase H in the deeper parts of the lower mantle. Fe^{3+}-rich compositions of phase H may further be stabilized by the spin transition to temperatures that exceed those of the ambient mantle. Fe-rich regions in the lower mantle may therefore have the highest potential for storing H_2O in phase H. However, while our thermodynamic analysis suggests a link between ferric iron and the storage of H_2O in phase H, further experiments are needed to directly determine the stability limits of Fe^{3+}-bearing phase H and other phase H components at pressures and temperatures of the lower mantle and for phase assemblages that reflect those in lower-mantle rocks. Our results indicate that such experiments may reveal an unexpectedly wide stability field of Fe^{3+}-bearing phase H at conditions of the lower mantle.

Appendix A: Debye Temperature and Partial Phonon Density of States

Nuclear resonant inelastic X-ray scattering (NRIXS) selectively interacts with vibrations of ^{57}Fe atoms. The projected partial phonon densities of states (p^3DOS) in Figure 4 therefore represent the contributions of vibrations of ^{57}Fe atoms to the total phonon density of states. The total phonon density of states $G(E)$ may be described as the sum of the partial phonon densities of states $g_j(E)$ of all atomic species j in a compound weighted by their atomic fractions a_j:

$$G(E) = \sum_j a_j g_j(E). \tag{A1}$$

The atomic fraction a_j is equal to the stoichiometric index s_j of an atomic species in the chemical formula of the compound divided by the total number $N = \sum_j s_j$ of atoms in the chemical formula, that is, $a_j = s_j/N$.

In Debye's approximation (e.g., Poirier, 2000), the phonon density of states is given by:

$$G(E) = D\omega^2 \frac{N}{v_D^3} \tag{A2}$$

and increases with the squared frequency ω^2 of lattice vibrations up to the Debye frequency $\omega_D = k_D v_D$. The velocity v_D is referred to as the Debye velocity and describes the slope of the linear dispersion curve up to the wave vector k_D, which defines the radius of the Brillouin zone. The constant D depends on the crystal structure and the volume of the crystal. The Debye temperature θ as the central parameter of the Debye model for vibrational properties is directly proportional to the Debye frequency ω_D and hence to the Debye velocity v_D:

$$\theta = \frac{\hbar}{k}\omega_D = \frac{\hbar}{k} k_D v_D. \tag{A3}$$

If the p^3DOS of individual atomic species are approximated by functions analogous to Equation A2, the total phonon density of states may be written as:

$$G(E) = D\omega^2 \frac{N}{v_D^3} = D\omega^2 N \sum_j \frac{a_j}{v_{Dj}^3}. \quad \text{(A4)}$$

From Equations A4 and A3, it follows that the overall Debye temperature θ is given by the harmonic mean of the cubed individual Debye temperatures θ_j weighted by the respective atomic fractions a_j:

$$\frac{1}{\theta^3} = \sum_j \frac{a_j}{\theta_j^3}. \quad \text{(A5)}$$

If we assign individual Debye temperatures θ_i to each electronic state i of Fe^{3+} cations and an additional Debye temperature θ_δ to the remainder of the crystal structure, Equation 12 follows directly from Equation A5.

Acronyms

APD	Avalanche photodiode
DAC	Diamond anvil cell
EOS	Equation of state
NAM	Nominally anhydrous mineral
NRIXS	Nuclear resonant inelastic X-ray scattering
p^3DOS	Projected partial phonon density of states
panDAC	Panoramic diamond anvil cell
XRD	X-ray diffraction

Data Availability Statement

All data needed to evaluate the conclusions in this paper are presented in the paper and/or included in Supporting Information S1. Integrated X-ray diffraction profiles have been deposited under https://doi.org/10.5281/zenodo.15790795 (Buchen, Pardo, Dobrosavljevic, Chariton, et al., 2025). Nuclear resonant inelastic X-ray scattering spectra and the derived projected partial phonon density of states have been deposited under https://doi.org/10.5281/zenodo.15842827 (Buchen, Pardo, Dobrosavljevic, Sturhahn, et al., 2025).

Acknowledgments
J.B. was supported by National Science Foundation's (NSF) Collaborative Studies of the Earth's Deep Interior under EAR-1161046 and EAR-2009935 awarded to J. M.J. and by the European Union's Horizon 2020 research and innovation programme (ERC Grant 864877). This research used resources of the Advanced Photon Source (APS), a U.S. Department of Energy (DOE) Office of Science User Facility operated for the DOE Office of Science by Argonne National Laboratory under contract no. DE-AC02-06CH11357. Portions of this work were performed at GeoSoilEnviroCARS (The University of Chicago, Sector 13), Advanced Photon Source, Argonne National Laboratory. GeoSoilEnviroCARS is supported by the National Science Foundation—Earth Sciences (EAR-1634415). Beamlines 3-ID-B and 13-ID-D at APS were partially supported by COMPRES, the Consortium for Materials Properties Research in Earth Sciences under NSF cooperative agreement EAR-1606856. This research was partly supported by JSPS KAKENHI Grants (Numbers 23K19067 and 24K00735) awarded to T.I.. We thank two anonymous reviewers for their constructive comments, which helped to improve the quality of our manuscript. Open Access funding enabled and organized by Projekt DEAL.

References

Akahama, Y., & Kawamura, H. (2006). Pressure calibration of diamond anvil Raman gauge to 310 GPa. *Journal of Applied Physics*, *100*(4), 043516. https://doi.org/10.1063/1.2335683

Andrault, D., & Bolfan-Casanova, N. (2022). Mantle rain toward the Earth's surface: A model for the internal cycle of water. *Physics of the Earth and Planetary Interiors*, *322*, 106815. https://doi.org/10.1016/j.pepi.2021.106815

Andrault, D., Pesce, G., Bouhifd, M. A., Bolfan-Casanova, N., Hénot, J.-M., & Mezouar, M. (2014). Melting of subducted basalt at the core-mantle boundary. *Science*, *344*(6186), 892–895. https://doi.org/10.1126/science.1250466

Bindi, L., Nishi, M., Tsuchiya, J., & Irifune, T. (2014). Crystal chemistry of dense hydrous magnesium silicates: The structure of phase H, $MgSiH_2O_4$, synthesized at 45 GPa and 1000°C. *American Mineralogist*, *99*(8–9), 1802–1805. https://doi.org/10.2138/am.2014.4994

Bolfan-Casanova, N. (2005). Water in the Earth's mantle. *Mineralogical Magazine*, *69*(3), 229–257. https://doi.org/10.1180/0026461056930248

Bolfan-Casanova, N., Keppler, H., & Rubie, D. C. (2000). Water partitioning between nominally anhydrous minerals in the $MgO–SiO_2–H_2O$ system up to 24 GPa: Implications for the distribution of water in the Earth's mantle. *Earth and Planetary Science Letters*, *182*(3–4), 209–221. https://doi.org/10.1016/S0012-821X(00)00244-2

Bolfan-Casanova, N., Keppler, H., & Rubie, D. C. (2003). Water partitioning at 660 km depth and evidence for very low water solubility in magnesium silicate perovskite. *Geophysical Research Letters*, *30*(17), 1905. https://doi.org/10.1029/2003gl017182

Bolfan-Casanova, N., Mackwell, S., Keppler, H., McCammon, C., & Rubie, D. C. (2002). Pressure dependence of H solubility in magnesiowüstite up to 25 GPa: Implications for the storage of water in the Earth's lower mantle. *Geophysical Research Letters*, *29*(10), 89-1–89-4. https://doi.org/10.1029/2001gl014457

Brounce, M., Stolper, E., & Eiler, J. (2017). Redox variations in Mauna Kea lavas, the oxygen fugacity of the Hawaiian plume, and the role of volcanic gases in Earth's oxygenation. *Proceedings of the National Academy of Sciences of the United States of Ameirca*, *114*(34), 8997–9002. https://doi.org/10.1073/pnas.1619527114

Buchen, J. (2021). Seismic wave velocities in Earth's mantle from mineral elasticity. In H. Marquardt, M. Ballmer, S. Cottaar, & J. Konter (Eds.), *Mantle convection and surface expressions* (Vol. 263, pp. 51–95). American Geophysical Union. https://doi.org/10.1002/9781119528609.ch3

Buchen, J., Pardo, O. S., Dobrosavljevic, V. V., Chariton, S., Greenberg, E., & Jackson, J. M. (2025). Powder X-ray diffraction patterns of δ-(Al, Fe)OOH at high pressures and high temperatures (Version 1) [Dataset]. *Zenodo*. https://doi.org/10.5281/zenodo.15790795

Buchen, J., Pardo, O. S., Dobrosavljevic, V. V., Sturhahn, W., Toellner, T. S., & Jackson, J. M. (2025). Nuclear resonant inelastic X-ray scattering spectra of δ-(Al,Fe)OOH at high pressures (Version 1) [Dataset]. *Zenodo*. https://doi.org/10.5281/zenodo.15842827

Buchen, J., Sturhahn, W., Ishii, T., & Jackson, J. M. (2021). Vibrational anisotropy of δ-(Al,Fe)OOH single crystals as probed by nuclear resonant inelastic x-ray scattering. *European Journal of Mineralogy*, *33*(4), 485–502. https://doi.org/10.5194/ejm-33-485-2021

Burns, R. G. (1993). *Mineralogical applications of crystal field theory*. Cambridge University Press. https://doi.org/10.1017/CBO9780511524899

Catalli, K., Shim, S.-H., Prakapenka, V. B., Zhao, J., Sturhahn, W., Chow, P., et al. (2010). Spin state of ferric iron in $MgSiO_3$ perovskite and its effect on elastic properties. *Earth and Planetary Science Letters*, *289*(1–2), 68–75. https://doi.org/10.1016/j.epsl.2009.10.029

Chen, B., Jackson, J. M., Sturhahn, W., Zhang, D., Zhao, J., Wicks, J. K., & Murphy, C. A. (2012). Spin crossover equation of state and sound velocities of $(Mg_{0.65}Fe_{0.35})O$ ferropericlase to 140 GPa. *Journal of Geophysical Research*, *117*(B8), B08208. https://doi.org/10.1029/2012jb009162

Chenavas, J., Joubert, J. C., Capponi, J. J., & Marezio, M. (1973). Synthese de nouvelles phases denses d'oxyhydroxydes $M^{3+}OOH$ des metaux de la premiere serie de transition, en milieu hydrothermal à tres haute pression. *Journal of Solid State Chemistry*, *6*(1), 1–15. https://doi.org/10.1016/0022-4596(73)90199-0

Criniti, G., Boffa Ballaran, T., Kurnosov, A., Ishii, T., Rogmann, E.-M., Glazyrin, K., et al. (2025). Effect of chemistry on the compressibility and high-pressure structural evolution of the $CaFe_2O_4$-type aluminous silicate phase. *Physics of the Earth and Planetary Interiors*, *361*, 107331. https://doi.org/10.1016/j.pepi.2025.107331

Deng, J., Niu, H., Hu, J., Chen, M., & Stixrude, L. (2023). Melting of $MgSiO_3$ determined by machine learning potentials. *Physical Review B*, *107*(6), 064103. https://doi.org/10.1103/PhysRevB.107.064103

Dewaele, A., Torrent, M., Loubeyre, P., & Mezouar, M. (2008). Compression curves of transition metals in the Mbar range: Experiments and projector augmented-wave calculations. *Physical Review B*, *78*(10), 104102. https://doi.org/10.1103/PhysRevB.78.104102

Dixon, J. E., Leist, L., Langmuir, C., & Schilling, J.-G. (2002). Recycled dehydrated lithosphere observed in plume-influenced mid-ocean-ridge basalt. *Nature*, *420*(6914), 385–389. https://doi.org/10.1038/nature01215

Duan, Y., Sun, N., Wang, S., Li, X., Guo, X., Ni, H., et al. (2018). Phase stability and thermal equation of state of δ-AlOOH: Implication for water transportation to the Deep Lower Mantle. *Earth and Planetary Science Letters*, *494*, 92–98. https://doi.org/10.1016/j.epsl.2018.05.003

Fei, H., & Katsura, T. (2020). High water solubility of ringwoodite at mantle transition zone temperature. *Earth and Planetary Science Letters*, *531*, 115987. https://doi.org/10.1016/j.epsl.2019.115987

Fei, H., & Katsura, T. (2021). Water solubility in Fe-bearing wadsleyite at mantle transition zone temperatures. *Geophysical Research Letters*, *48*(9), e2021GL092836. https://doi.org/10.1029/2021GL092836

Fei, Y., Ricolleau, A., Frank, M., Mibe, K., Shen, G., & Prakapenka, V. (2007). Toward an internally consistent pressure scale. *Proceedings of the National Academy of Sciences United States of America*, *104*(22), 9182–9186. https://doi.org/10.1073/pnas.0609013104

Fiquet, G., Auzende, A. L., Siebert, J., Corgne, A., Bureau, H., Ozawa, H., & Garbarino, G. (2010). Melting of peridotite to 140 gigapascals. *Science*, *329*(5998), 1516–1518. https://doi.org/10.1126/science.1192448

Frost, D. J., Liebske, C., Langenhorst, F., McCammon, C. A., Trønnes, R. G., & Rubie, D. C. (2004). Experimental evidence for the existence of iron-rich metal in the Earth's lower mantle. *Nature*, *428*(6981), 409–412. https://doi.org/10.1038/nature02413

Fu, S., Yang, J., Karato, S. I., Vasiliev, A., Presniakov, M. Y., Gavriliuk, A. G., et al. (2019). Water concentration in single-crystal (Al,Fe)-bearing bridgmanite grown from the hydrous melt: Implications for dehydration melting at the topmost lower mantle. *Geophysical Research Letters*, *46*(17–18), 10346–10357. https://doi.org/10.1029/2019gl084630

Ghosh, S., & Schmidt, M. W. (2014). Melting of phase D in the lower mantle and implications for recycling and storage of H_2O in the deep mantle. *Geochimica et Cosmochimica Acta*, *145*, 72–88. https://doi.org/10.1016/j.gca.2014.06.025

Glazyrin, K., Boffa Ballaran, T., Frost, D. J., McCammon, C., Kantor, A., Merlini, M., et al. (2014). Magnesium silicate perovskite and effect of iron oxidation state on its bulk sound velocity at the conditions of the lower mantle. *Earth and Planetary Science Letters*, *393*, 182–186. https://doi.org/10.1016/j.epsl.2014.01.056

Gleason, A. E., Quiroga, C. E., Suzuki, A., Pentcheva, R., & Mao, W. L. (2013). Symmetrization driven spin transition in ε-FeOOH at high pressure. *Earth and Planetary Science Letters*, *379*, 49–55. https://doi.org/10.1016/j.epsl.2013.08.012

Hirschmann, M. M. (2006). Water, melting, and the deep Earth H_2O cycle. *Annual Review of Earth and Planetary Sciences*, *34*(1), 629–653. https://doi.org/10.1146/annurev.earth.34.031405.125211

Holtgrewe, N., Greenberg, E., Prescher, C., Prakapenka, V. B., & Goncharov, A. F. (2019). Advanced integrated optical spectroscopy system for diamond anvil cell studies at GSECARS. *High Pressure Research*, *39*(3), 457–470. https://doi.org/10.1080/08957959.2019.1647536

Hsu, H. (2017). First-principles study of iron spin crossover in the new hexagonal aluminous phase. *Physical Review B*, *95*(2), 020406. https://doi.org/10.1103/PhysRevB.95.020406

Hsu, H., Blaha, P., Cococcioni, M., & Wentzcovitch, R. M. (2011). Spin-state crossover and hyperfine interactions of ferric iron in $MgSiO_3$ perovskite. *Physical Review Letters*, *106*(11), 118501. https://doi.org/10.1103/PhysRevLett.106.118501

Hsu, H., Yu, Y. G., & Wentzcovitch, R. M. (2012). Spin crossover of iron in aluminous $MgSiO_3$ perovskite and post-perovskite. *Earth and Planetary Science Letters*, *359–360*, 34–39. https://doi.org/10.1016/j.epsl.2012.09.029

Irifune, T., Shinmei, T., McCammon, C. A., Miyajima, N., Rubie, D. C., & Frost, D. J. (2010). Iron partitioning and density changes of pyrolite in Earth's lower mantle. *Science*, *327*(5962), 193–195. https://doi.org/10.1126/science.1181443

Ishii, T., Criniti, G., Purevjav, N., Katsura, T., & Ohtani, E. (2024). Hydrogen partitioning between stishovite and hydrous phase δ: Implications for water cycle and distribution in the lower mantle. *Progress in Earth and Planetary Science*, *11*(1), 10. https://doi.org/10.1186/s40645-024-00615-0

Ishii, T., Miyajima, N., Criniti, G., Hu, Q., Glazyrin, K., & Katsura, T. (2022). High pressure-temperature phase relations of basaltic crust up to mid-mantle conditions. *Earth and Planetary Science Letters*, *584*, 117472. https://doi.org/10.1016/j.epsl.2022.117472

Ishii, T., Ohtani, E., & Shatskiy, A. (2022). Aluminum and hydrogen partitioning between bridgmanite and high-pressure hydrous phases: Implications for water storage in the lower mantle. *Earth and Planetary Science Letters*, *583*, 117441. https://doi.org/10.1016/j.epsl.2022.117441

Ita, J., & Stixrude, L. (1992). Petrology, elasticity, and composition of the mantle transition zone. *Journal of Geophysical Research*, *97*(B5), 6849–6866. https://doi.org/10.1029/92JB00068

Karato, S.-I., Karki, B., & Park, J. (2020). Deep mantle melting, global water circulation and its implications for the stability of the ocean mass. *Progress in Earth and Planetary Science*, *7*(1), 76. https://doi.org/10.1186/s40645-020-00379-3

Katsura, T. (2022). A revised adiabatic temperature profile for the mantle. *Journal of Geophysical Research: Solid Earth*, *127*(2), e2021JB023562. https://doi.org/10.1029/2021jb023562

Kawazoe, T., Ohira, I., Ishii, T., Boffa Ballaran, T., McCammon, C., Suzuki, A., & Ohtani, E. (2017). Single crystal synthesis of δ-(Al,Fe)OOH. *American Mineralogist*, *102*(9), 1953–1956. https://doi.org/10.2138/am-2017-6153

Kohlstedt, D. L., Keppler, H., & Rubie, D. C. (1996). Solubility of water in the α, β and γ phases of $(Mg,Fe)_2SiO_4$. *Contributions to Mineralogy and Petrology*, *123*(4), 345–357. https://doi.org/10.1007/s004100050161

Kohn, V. G., & Chumakov, A. I. (2000). DOS: Evaluation of phonon density of states from nuclear resonant inelastic absorption. *Hyperfine Interactions*, *125*(1–4), 205–221. https://doi.org/10.1023/A:1012689705503

Komabayashi, T., & Omori, S. (2006). Internally consistent thermodynamic data set for dense hydrous magnesium silicates up to 35 GPa, 1600°C: Implications for water circulation in the Earth's deep mantle. *Physics of the Earth and Planetary Interiors*, *156*(1–2), 89–107. https://doi.org/10.1016/j.pepi.2006.02.002

Komatsu, K., Kuribayashi, T., Sano, A., Ohtani, E., & Kudoh, Y. (2006). Redetermination of the high-pressure modification of AlOOH from single-crystal synchrotron data. *Acta Crystallographica*, *E62*(11), i216–i218. https://doi.org/10.1107/s160053680603916x

Lin, J. F., Jacobsen, S. D., Sturhahn, W., Jackson, J. M., Zhao, J., & Yoo, C. S. (2006). Sound velocities of ferropericlase in the Earth's lower mantle. *Geophysical Research Letters*, *33*(22), L22304. https://doi.org/10.1029/2006gl028099

Lin, J. F., Mao, Z., Yang, J., Liu, J., Xiao, Y., Chow, P., & Okuchi, T. (2016). High-spin Fe^{2+} and Fe^{3+} in single-crystal aluminous bridgmanite in the lower mantle. *Geophysical Research Letters*, *43*(13), 6952–6959. https://doi.org/10.1002/2016gl069836

Litasov, K., Ohtani, E., Langenhorst, F., Yurimoto, H., Kubo, T., & Kondo, T. (2003). Water solubility in Mg-perovskites and water storage capacity in the lower mantle. *Earth and Planetary Science Letters*, *211*(1–2), 189–203. https://doi.org/10.1016/s0012-821x(03)00200-0

Liu, H., Hu, J., Xu, J., Liu, Z., Shu, J., Mao, H. K., & Chen, J. (2004). Phase transition and compression behavior of gibbsite under high-pressure. *Physics and Chemistry of Minerals*, *31*(4), 240–246. https://doi.org/10.1007/s00269-004-0390-2

Liu, J., Dorfman, S. M., Zhu, F., Li, J., Wang, Y., Zhang, D., et al. (2018). Valence and spin states of iron are invisible in Earth's lower mantle. *Nature Communications*, *9*(1), 1284. https://doi.org/10.1038/s41467-018-03671-5

Liu, Z., Fei, H., Chen, L., McCammon, C., Wang, L., Liu, R., et al. (2021). Bridgmanite is nearly dry at the top of the lower mantle. *Earth and Planetary Science Letters*, *570*, 117088. https://doi.org/10.1016/j.epsl.2021.117088

Moussallam, Y., Longpré, M.-A., McCammon, C., Gomez-Ulla, A., Rose-Koga, E. F., Scaillet, B., et al. (2019). Mantle plumes are oxidised. *Earth and Planetary Science Letters*, *527*, 115798. https://doi.org/10.1016/j.epsl.2019.115798

Nishi, M., Irifune, T., Gréaux, S., Tange, Y., & Higo, Y. (2015). Phase transitions of serpentine in the lower mantle. *Physics of the Earth and Planetary Interiors*, *245*, 52–58. https://doi.org/10.1016/j.pepi.2015.05.007

Nishi, M., Irifune, T., Tsuchiya, J., Tange, Y., Nishihara, Y., Fujino, K., & Higo, Y. (2014). Stability of hydrous silicate at high pressures and water transport to the deep lower mantle. *Nature Geoscience*, *7*(3), 224–227. https://doi.org/10.1038/ngeo2074

Nishi, M., Kuwayama, Y., Tsuchiya, J., & Tsuchiya, T. (2017). The pyrite-type high-pressure form of FeOOH. *Nature*, *547*(7662), 205–208. https://doi.org/10.1038/nature22823

Nishi, M., Tsuchiya, J., Arimoto, T., Kakizawa, S., Kunimoto, T., Tange, Y., et al. (2018). Thermal equation of state of $MgSiO_4H_2$ phase H determined by in situ X-ray diffraction and a multianvil apparatus. *Physics and Chemistry of Minerals*, *45*(10), 995–1001. https://doi.org/10.1007/s00269-018-0980-z

Nishi, M., Tsuchiya, J., Kuwayama, Y., Arimoto, T., Tange, Y., Higo, Y., et al. (2019). Solid solution and compression behavior of hydroxides in the lower mantle. *Journal of Geophysical Research: Solid Earth*, *124*(10), 10231–10239. https://doi.org/10.1029/2019jb018146

Nomura, R., Hirose, K., Uesugi, K., Ohishi, Y., Tsuchiyama, A., Miyake, A., & Ueno, Y. (2014). Low core-mantle boundary temperature inferred from the solidus of pyrolite. *Science*, *343*(6170), 522–525. https://doi.org/10.1126/science.1248186

Ohira, I., Jackson, J. M., Solomatova, N. V., Sturhahn, W., Finkelstein, G. J., Kamada, S., et al. (2019). Compressional behavior and spin state of δ-(Al,Fe)OOH at high pressures. *American Mineralogist*, *104*(9), 1273–1284. https://doi.org/10.2138/am-2019-6913

Ohira, I., Jackson, J. M., Sturhahn, W., Finkelstein, G. J., Kawazoe, T., Toellner, T. S., et al. (2021). The influence of δ-(Al,Fe)OOH on seismic heterogeneities in Earth's lower mantle. *Scientific Reports*, *11*(1), 12036. https://doi.org/10.1038/s41598-021-91180-9

Ohira, I., Ohtani, E., Sakai, T., Miyahara, M., Hirao, N., Ohishi, Y., & Nishijima, M. (2014). Stability of a hydrous δ-phase, AlOOH–$MgSiO_2(OH)_2$, and a mechanism for water transport into the base of lower mantle. *Earth and Planetary Science Letters*, *401*, 12–17. https://doi.org/10.1016/j.epsl.2014.05.059

Ohtani, E. (2015). Hydrous minerals and the storage of water in the deep mantle. *Chemical Geology*, *418*, 6–15. https://doi.org/10.1016/j.chemgeo.2015.05.005

Ohtani, E. (2021). Hydration and dehydration in Earth's interior. *Annual Review of Earth and Planetary Sciences*, *49*(1), 253–278. https://doi.org/10.1146/annurev-earth-080320-062509

Ohtani, E., Amaike, Y., Kamada, S., Sakamaki, T., & Hirao, N. (2014). Stability of hydrous phase H $MgSiO_4H_2$ under lower mantle conditions. *Geophysical Research Letters*, *41*(23), 8283–8287. https://doi.org/10.1002/2014gl061690

Ohtani, E., & Ishii, T. (2024). Role of water in dynamics of slabs and surrounding mantle. *Progress in Earth and Planetary Science*, *11*(1), 65. https://doi.org/10.1186/s40645-024-00670-7

Ohtani, E., Litasov, K., Hosoya, T., Kubo, T., & Kondo, T. (2004). Water transport into the deep mantle and formation of a hydrous transition zone. *Physics of the Earth and Planetary Interiors*, *143–144*, 255–269. https://doi.org/10.1016/j.pepi.2003.09.015

Pamato, M. G., Myhill, R., Boffa Ballaran, T., Frost, D. J., Heidelbach, F., & Miyajima, N. (2014). Lower-mantle water reservoir implied by the extreme stability of a hydrous aluminosilicate. *Nature Geoscience*, *8*(1), 75–79. https://doi.org/10.1038/ngeo2306

Panero, W. R., Pigott, J. S., Reaman, D. M., Kabbes, J. E., & Liu, Z. (2015). Dry $(Mg,Fe)SiO_3$ perovskite in the Earth's lower mantle. *Journal of Geophysical Research: Solid Earth*, *120*(2), 894–908. https://doi.org/10.1002/2014jb011397

Pernet, M., Joubert, J. C., & Berthet-Colominas, C. (1975). Etude par diffraction neutronique de la forme haute pression de FeOOH. *Solid State Communications*, *17*(12), 1505–1510. https://doi.org/10.1016/0038-1098(75)90983-7

Peslier, A. H., Schönbächler, M., Busemann, H., & Karato, S.-I. (2017). Water in the Earth's interior: Distribution and origin. *Space Science Reviews*, *212*(1–2), 743–810. https://doi.org/10.1007/s11214-017-0387-z

Piet, H., Leinenweber, K. D., Tappan, J., Greenberg, E., Prakapenka, V. B., Buseck, P. R., & Shim, S.-H. (2020). Dehydration of δ-AlOOH in Earth's deep lower mantle. *Minerals*, *10*(4), 384. https://doi.org/10.3390/min10040384

Poirier, J.-P. (2000). *Introduction to the physics of the Earth's interior*. Cambridge University Press. https://doi.org/10.1017/CBO9781139164467

Prescher, C. (2016). T-Rax (Version 1.1) [Software]. *GitHub*. Retrieved from www.github.com/CPrescher/T-Rax

Prescher, C. (2019–2020). DIOPTAS (Versions 0.5.0 to 0.5.2) [Software]. *GitHub*. Retrieved from www.github.com/Dioptas/Dioptas

Prescher, C., & Prakapenka, V. B. (2015). DIOPTAS: A program for reduction of two-dimensional X-ray diffraction data and data exploration. *High Pressure Research*, *35*(3), 223–230. https://doi.org/10.1080/08957959.2015.1059835

Robie, R. A., Hemingway, B. S., & Fisher, J. R. (1978). *Thermodynamic properties of minerals and related substances at 298.15 K and 1 bar (10^5 Pascals) pressure and at higher temperatures*. United States Geological Survey Bulletin. No. 1452.

Rodríguez-Carvajal, J. (1993). Recent advances in magnetic structure determination by neutron powder diffraction. *Physica B*, *192*(1–2), 55–69. https://doi.org/10.1016/0921-4526(93)90108-I

Rodríguez-Carvajal, J. (2020). FullProf (Version 2.6.2) [Software]. Retrieved from www.ill.eu/sites/fullprof/index.html
Sano, A., Ohtani, E., Kondo, T., Hirao, N., Sakai, T., Sata, N., et al. (2008). Aluminous hydrous mineral δ-AlOOH as a carrier of hydrogen into the core-mantle boundary. *Geophysical Research Letters*, *35*(3), L03303. https://doi.org/10.1029/2007gl031718
Sano-Furukawa, A., Hattori, T., Komatsu, K., Kagi, H., Nagai, T., Molaison, J. J., et al. (2018). Direct observation of symmetrization of hydrogen bond in δ-AlOOH under mantle conditions using neutron diffraction. *Scientific Reports*, *8*(1), 15520. https://doi.org/10.1038/s41598-018-33598-2
Sano-Furukawa, A., Kagi, H., Nagai, T., Nakano, S., Fukura, S., Ushijima, D., et al. (2009). Change in compressibility of δ-AlOOH and δ-AlOOD at high pressure: A study of isotope effect and hydrogen-bond symmetrization. *American Mineralogist*, *94*(8–9), 1255–1261. https://doi.org/10.2138/am.2009.3109
Satta, N., Criniti, G., Kurnosov, A., Ballaran, T. B., Ishii, T., & Marquardt, H. (2024). Elastic anomalies across the $P2_1nm \rightarrow Pnnm$ structural phase transition in δ-(Al,Fe)OOH. *American Mineralogist*, *109*(11), 1934–1944. https://doi.org/10.2138/am-2023-9129
Stixrude, L., & Karki, B. (2005). Structure and freezing of $MgSiO_3$ liquid in Earth's lower mantle. *Science*, *310*(5746), 297–299. https://doi.org/10.1126/science.1116952
Stixrude, L., & Lithgow-Bertelloni, C. (2005). Thermodynamics of mantle minerals—I. Physical properties. *Geophysical Journal International*, *162*(2), 610–632. https://doi.org/10.1111/j.1365-246X.2005.02642.x
Stixrude, L., & Lithgow-Bertelloni, C. (2024). Thermodynamics of mantle minerals—III: The role of iron. *Geophysical Journal International*, *237*(3), 1699–1733. https://doi.org/10.1093/gji/ggae126
Strozewski, B., Buchen, J., Sturhahn, W., Ishii, T., Ohira, I., Chariton, S., et al. (2023). Equation of state and spin crossover of (Al, Fe)-phase H. *Journal of Geophysical Research: Solid Earth*, *128*(4), e2022JB026291. https://doi.org/10.1029/2022jb026291
Sturhahn, W. (2000). CONUSS and PHOENIX: Evaluation of nuclear resonant scattering data. *Hyperfine Interactions*, *125*(1–4), 149–172. https://doi.org/10.1023/A:1012681503686
Sturhahn, W. (2004). Nuclear resonant spectroscopy. *Journal of Physics: Condensed Matter*, *16*(5), S497–S530. https://doi.org/10.1088/0953-8984/16/5/009
Sturhahn, W. (2021a). MINUTI (Version 2.2.1) [Software]. Retrieved from www.nrixs.com
Sturhahn, W. (2021b). PHOENIX (Version 3.0.4) [Software]. Retrieved from www.nrixs.com
Sturhahn, W., Jackson, J. M., & Lin, J.-F. (2005). The spin state of iron in minerals of Earth's lower mantle. *Geophysical Research Letters*, *32*(12), L12307. https://doi.org/10.1029/2005gl022802
Sturhahn, W., & Kohn, V. G. (1999). Theoretical aspects of incoherent nuclear resonant scattering. *Hyperfine Interactions*, *123*(1–4), 367–399. https://doi.org/10.1023/A:1017071806895
Su, X., Zhao, C., Lv, C., Zhuang, Y., Salke, N., Xu, L., et al. (2021). The effect of iron on the sound velocities of δ-AlOOH up to 135 GPa. *Geoscience Frontiers*, *12*(2), 937–946. https://doi.org/10.1016/j.gsf.2020.08.012
Su, X., Zhao, C., Xu, L., Lv, C., Song, X., Ishii, T., et al. (2021). Spectroscopic evidence for the Fe^{3+} spin transition in iron-bearing δ-AlOOH at high pressure. *American Mineralogist*, *106*(11), 1709–1716. https://doi.org/10.2138/am-2021-7541
Suzuki, A. (2010). High-pressure X-ray diffraction study of ε-FeOOH. *Physics and Chemistry of Minerals*, *37*(3), 153–157. https://doi.org/10.1007/s00269-009-0319-x
Suzuki, A., Ohtani, E., & Kamada, T. (2000). A new hydrous phase δ-AlOOH synthesized at 21 GPa and 1000°C. *Physics and Chemistry of Minerals*, *27*(10), 689–693. https://doi.org/10.1007/s002690000120
Tanabe, Y., & Sugano, S. (1954). On the absorption spectra of complex ions. I. *Journal of the Physical Society of Japan*, *9*(5), 753–766. https://doi.org/10.1143/JPSJ.9.753
Thompson, E. C., Davis, A. H., Brauser, N. M., Liu, Z., Prakapenka, V. B., & Campbell, A. J. (2020). Phase transitions in ε-FeOOH at high pressure and ambient temperature. *American Mineralogist*, *105*(12), 1769–1777. https://doi.org/10.2138/am-2020-7468
Toellner, T. S. (2000). Monochromatization of synchrotron radiation for nuclear resonant scattering experiments. *Hyperfine Interactions*, *125*(1–4), 3–28. https://doi.org/10.1023/A:1012621317798
Walter, M. J., Thomson, A. R., Wang, W., Lord, O. T., Ross, J., McMahon, S. C., et al. (2015). The stability of hydrous silicates in Earth's lower mantle: Experimental constraints from the systems $MgO–SiO_2–H_2O$ and $MgO–Al_2O_3–SiO_2–H_2O$. *Chemical Geology*, *418*, 16–29. https://doi.org/10.1016/j.chemgeo.2015.05.001
Wang, W., Liu, J., Yang, H., Dorfman, S. M., Lv, M., Li, J., et al. (2021). Iron force constants of bridgmanite at high pressure: Implications for iron isotope fractionation in the deep mantle. *Geochimica et Cosmochimica Acta*, *294*, 215–231. https://doi.org/10.1016/j.gca.2020.11.025
Weis, D., Harpp, K. S., Harrison, L. N., Boyet, M., Chauvel, C., Farnetani, C. G., et al. (2023). Earth's mantle composition revealed by mantle plumes. *Nature Reviews Earth & Environment*, *4*(9), 604–625. https://doi.org/10.1038/s43017-023-00467-0
Wentzcovitch, R. M., Justo, J. F., Wu, Z., da Silva, C. R. S., Yuen, D. A., & Kohlstedt, D. (2009). Anomalous compressibility of ferropericlase throughout the iron spin cross-over. *Proceedings of the National Academy of Sciences United States of America*, *106*(21), 8447–8452. https://doi.org/10.1073/pnas.0812150106
Wu, Y., Qin, F., Wu, X., Huang, H., McCammon, C. A., Yoshino, T., et al. (2017). Spin transition of ferric iron in the calcium-ferrite type aluminous phase. *Journal of Geophysical Research: Solid Earth*, *122*(8), 5935–5944. https://doi.org/10.1002/2017jb014095
Wu, Y., Wu, X., Lin, J.-F., McCammon, C. A., Xiao, Y., Chow, P., et al. (2016). Spin transition of ferric iron in the NAL phase: Implications for the seismic heterogeneities of subducted slabs in the lower mantle. *Earth and Planetary Science Letters*, *434*, 91–100. https://doi.org/10.1016/j.epsl.2015.11.011
Wu, Z., Justo, J. F., da Silva, C. R. S., de Gironcoli, S., & Wentzcovitch, R. M. (2009). Anomalous thermodynamic properties in ferropericlase throughout its spin crossover. *Physical Review B*, *80*(1), 014409. https://doi.org/10.1103/PhysRevB.80.014409
Xu, C., Nishi, M., & Inoue, T. (2019). Solubility behavior of δ-AlOOH and ε-FeOOH at high pressures. *American Mineralogist*, *104*(10), 1416–1420. https://doi.org/10.2138/am-2019-7064
Yang, H., Lin, J.-F., Hu, M. Y., Roskosz, M., Bi, W., Zhao, J., et al. (2019). Iron isotopic fractionation in mineral phases from Earth's lower mantle: Did terrestrial magma ocean crystallization fractionate iron isotopes? *Earth and Planetary Science Letters*, *506*, 113–122. https://doi.org/10.1016/j.epsl.2018.10.034
Yuan, H., Zhang, L., Ohtani, E., Meng, Y., Greenberg, E., & Prakapenka, V. B. (2019). Stability of Fe-bearing hydrous phases and element partitioning in the system $MgO–Al_2O_3–Fe_2O_3–SiO_2–H_2O$ in Earth's lowermost mantle. *Earth and Planetary Science Letters*, *524*, 115714. https://doi.org/10.1016/j.epsl.2019.115714